Simulating growth of TDP-43 cytosolic inclusion bodies in neurons

Andrey V. Kuznetsov

Department of Mechanical and Aerospace Engineering, North Carolina State University,

Raleigh, NC 27695-7910, USA; e-mail: avkuznet@ncsu.edu

Abstract

This paper introduces a mathematical model for the growth of transactive response DNA binding protein of 43 kDa (TDP-43) inclusion bodies in neuron soma. The model's equations enable numerical determination of the concentrations of TDP-43 dimers, monomers, and aggregates. Assuming all aggregates integrate into the inclusion bodies, the model predicts the size of TDP-43 inclusion bodies. An approximate solution to the model equations is derived for the scenario in which protein degradation machinery is dysfunctional, resulting in infinite half-lives for TDP-43 dimers, monomers, and aggregates. This solution, valid for large times, predicts that the inclusion body's radius increases proportionally to the cube root of time. To the best of the author's knowledge, this study presents the first attempt to model the relationship between the size of TDP-43 inclusion bodies and time. The sensitivity analysis of the approximate solution indicates that the concentrations of TDP-43 monomers and aggregates, as well as inclusion body radii, are independent of the kinetic constants. While the numerical solution of the full mathematical model continues to work with finite half-lives, the approximate solution becomes invalid for scenarios with physiologically relevant (finite) half-lives of TDP-43 dimers, monomers, and aggregates. In contrast to the situation with infinite half-lives, the numerical solution shows that for various values of kinetic constants, the curves representing concentrations of monomers and aggregates, as well as the curves depicting inclusion body radii, converge to distinct constant values.

Keywords neuron; amyotrophic lateral sclerosis; frontotemporal lobar degeneration; Finke-Watzky model; mathematical modeling

Abbreviations

ALS amyotrophic lateral sclerosis

F-W Finke-Watzky

FTLD frontotemporal lobar degeneration

TDP-43 transactive response DNA binding protein of 43 kDa

1. Introduction

The presence of transactive response DNA binding protein of 43 kDa (TDP-43) inclusion bodies represents a pathological hallmark in amyotrophic lateral sclerosis (ALS) and frontotemporal lobar degeneration (FTLD) diseases (Ishii et al. 2017; Jo et al. 2020; Prasad et al. 2019; Capitini et al. 2014). ALS is distinguished by the gradual decline of motor neurons, resulting in skeletal muscle weakness and, ultimately, fatality within a span of 3 to 5 years (Oiwa et al. 2023; Sugai et al. 2018). FTLD is early-onset neurodegenerative disease characterized by progressive deterioration in behavior and language due to the loss of neurons, primarily in the frontal or temporal lobes, with a life expectancy of 6-8 years (Grossman et al. 2023). TDP-43, a nuclear, intrinsically disordered, soluble protein (Sun et al. 2019; French et al. 2019) with a molecular weight of 43 kDa (Suk and Rousseaux 2020), is synthesized in the cytoplasm and, in healthy neurons, predominantly resides in the nucleus (Pérez-Berlanga et al. 2023; Necarsulmer et al. 2023; Meneses et al. 2021). Degradation of TDP-43 occurs through both proteasomal and autophagy pathways (Chhangani et al. 2021). However, in TDP-43 proteinopathies, this protein undergoes mislocalization from the nucleus to the cytoplasm (Glass 2020; Suk and Rousseaux 2020), forming TDP-43 inclusion bodies characterized by ubiquitinated and hyper-phosphorylated variants of TDP-43 (Prasad et al. 2019).

Under pathological conditions, TDP-43 undergoes a conversion from its native dimeric state (Jiang et al. 2017) to a monomeric form. This transformation results in TDP-43 mislocalization from the nucleus to the cytoplasm, where it forms irreversible, amorphous aggregates (Sun et al. 2014; Oiwa et al. 2023). Subsequently, these aggregates grow into inclusion bodies. Notably, the nature of these inclusion bodies, whether they exhibit toxicity or act in a neuroprotective manner by sequestering toxic soluble oligomers, remains uncertain (Ishii et al. 2017; Glass 2020). There is a possibility that TDP-43 pathology spreads between neurons through a prion-like mechanism (Jo et al. 2020; Chong and Forman-Kay 2016).

This paper develops a model for TDP-43 inclusion body growth, predicting the correlation between the radius of the inclusion body and time. This builds upon the author's previous research, which explored the growth of amyloid-β plaques (Kuznetsov 2024b) and Lewy bodies (Kuznetsov and Kuznetsov 2022; Kuznetsov 2024a). The growth of TDP-43 inclusion bodies is simulated using the methodology developed in Kuznetsov (2024a), Kuznetsov (2024b). The model includes equations that describe the conservation of TDP-43 monomers, dimers, and aggregates. The conversion of dimers into aggregates is simulated using the Finke-Watzky model.

2. Materials and models

2.1. Governing equations

According to Oiwa et al. (2023), the initial stage of TDP-43 aggregation involves the monomerization of TDP-43 dimers:

$$D \xrightarrow{k_M} 2M\,. \tag{1}$$

To simulate TDP-43 aggregation, a phenomenological two-step Finke-Watzky (F-W) model, as described in Morris et al. (2008), Iashchishyn et al. (2017), was employed. The F-W model, which has been successfully applied to fit experimental data on neurological protein aggregation (Morris et al. 2008), simulates polymer aggregation through two pseudoelementary, parallel, and competing processes: continuous nucleation and autocatalytic surface growth (Finke et al. 2020). The F-W model is characterized by the following transitions:

$$M \xrightarrow{k_1} B\,, \tag{2}$$

$$M + B \xrightarrow{k_2} 2B\,. \tag{3}$$

The mathematical model is derived by establishing three conservation statements for dimers, monomers, and aggregates. The model utilizes the lumped capacitance approximation, making time, *t*, the sole independent variable. The dependent variables are listed in Table 1, and the model parameters are summarized in Table 2.

The conservation of TDP-43 dimers in the soma is expressed by the following equation:

$$\frac{d[D]}{dt} = \frac{q_D}{V_{soma}} a_{21} - k_M [D] - [D] \frac{\ln(2)}{T_{1/2,D}}\,. \tag{4}$$

In Eq. (4), $a_{21} = 10^{21} \frac{\mu\text{M}\ \mu\text{m}^3}{\text{mol}}$ represents the conversion factor from $\frac{\text{mol}}{\mu\text{m}^3}$ to μM. The first term on the right-hand side of Eq. (4) simulates the rate at which TDP-43 dimers, a native form of TDP-43, are produced in the soma. The second term is formulated by applying the law of mass action to describe the rate of reaction in Eq. (1). The third term simulates the degradation of TDP-43 dimers due to their finite half-life.

The conservation of TDP-43 monomers in the soma is described by the following equation:

$$\frac{d[M]}{dt} = 2k_M[D] - k_1[M] - k_2[M][B] - [M]\frac{\ln(2)}{T_{1/2,M}}, \tag{5}$$

where the first term on the right-hand side describes the generation of TDP-43 monomers through their conversion from dimers. The second term simulates the decrease of monomer concentration resulting from their transformation into the misfolded active form capable of autocatalysis. In the F-W model, this process is conceptualized as a nucleation process (refer to Eq. (2)). The third term accounts for the decrease of monomer concentration due to autocatalytic conversion into their aggregated form (refer to Eq. (3)). The fourth term represents the degradation of TDP-43 monomers due to their finite half-life.

By expressing the conservation of TDP-43 aggregates, the following is derived:

$$\frac{d[B]}{dt} = k_1[M] + k_2[M][B] - [B]\frac{\ln(2)}{T_{1/2,B}}. \tag{6}$$

The first and second terms on the right-hand side of Eq. (6) simulate the generation of TDP-43 aggregates resulting from their production from monomers through nucleation and autocatalytic processes, respectively. The third term on the right-hand side represents the decline of TDP-43 aggregates due to their limited half-life. The existing model does not simulate the mechanism of sticky TDP-43 aggregates coming together to form the inclusion bodies. It is presumed that this assembly process occurs more rapidly than the formation of TDP-43 aggregates in the soma.

Eqs. (4)-(6) are solved with the following initial conditions:

At $t = 0$: $\quad [D] = [D]_0, \quad [M] = 0, \quad [B] = 0.$ (7a,b,c)

Table 1. Dependent variables in the model.

Symbol	Definition	Unit
$[B]$	Molar concentration of the misfolded form of TDP-43 prone to aggregation	μM
$[D]$	Molar concentration of TDP-43 dimers, representing the native form of TDP-43	μM
$[M]$	Molar concentration of TDP-43 monomers	μM

r_{IB}	Radius of the growing inclusion body, assuming it takes on a spherical form	μm

Table 2. Model parameters along with their estimated values.

Symbol	Definition	Unit	Value or range	Reference or estimation method	Value(s) used in computations
a_{21}	Conversion factor from $\frac{\text{mol}}{\mu\text{m}^3}$ to μM	$\frac{\mu\text{M}\ \mu\text{m}^3}{\text{mol}}$	10^{21}		10^{21}
$[D]_0$	Initial concentration of TDP-43 dimers	μM			0 [a]
D_{soma}	Diameter of the soma	μm	20 [b]		20
D_{IB}	Diameter of a mature spherical TDP-43 inclusion body	μm	1-25 μm [c]	Cascella et al. (2022)	8
k_1	Rate constant associated with the first pseudoelementary step in the F-W model that describes the nucleation of the misfolded form of TDP-43 prone to aggregation	s^{-1}			10^{-4}, 10^{-6}, 10^{-8} [d]
k_2	Rate constant associated with the second pseudoelementary	$\mu M^{-1}\ s^{-1}$			10^{-4}, 10^{-6}, 10^{-8} [e]

	step of the F-W model that describes the autocatalytic growth of the misfolded form of TDP-43 prone to aggregation				
k_M	Rate constant associated with the reaction that describes the conversion of TDP-43 dimers into monomers	s^{-1}			10^{-2}, 10^{-4}, 10^{-6} [f]
MW	Molecular weight of TDP-43 monomer	$g\ mol^{-1}$	4.3×10^{4} [g]	Suk and Rousseaux (2020), Meneses et al. (2021), Hadley et al. (2015)	4.3×10^{4}
N_A	Avogadro's number	mol^{-1}	6.022×10^{23}		6.022×10^{23}
N_{IB}	Number of mature TDP-43 inclusion bodies within the soma (assumed to be of the same volume)		0-4 [h]	Ishii et al. (2017)	2
q_D	Rate at which TDP-43 dimers are generated within the soma	$mol\ s^{-1}$	6.68×10^{-23}	Estimated using Eq. (20)	6.68×10^{-23}

$t_{IB,f}$	Duration of TDP-43 inclusion body growth	s	1.26×10^{8} [i]	Prasad et al. (2019), Oiwa et al. (2023), Chhangani et al. (2021), Sugai et al. (2018)	1.26×10^{8}
$T_{1/2,B}$	Half-life of TDP-43 in the misfolded form prone to aggregation	s	8.64×10^{4} - 1.73×10^{5} [j]	Prasad et al. (2019)	1.30×10^{5}, 10^{20} (to simulate $T_{1/2,B}\rightarrow\infty$)
$T_{1/2,D}$	Half-life of TDP-43 dimers	s	4.32×10^{4} [k]	Ling et al. (2010), Prasad et al. (2019)	4.32×10^{4}, 10^{20} (to simulate $T_{1/2,D}\rightarrow\infty$)
$T_{1/2,M}$	Half-life of TDP-43 monomers	s	4.32×10^{4} [l]	Ling et al. (2010), Prasad et al. (2019)	4.32×10^{4}, 10^{20} (to simulate $T_{1/2,M}\rightarrow\infty$)
ρ_{IB}	Density of TDP-43 inclusion bodies	g/μm^3	1.35×10^{-12} [m]	Cavicchi et al. (2018)	1.35×10^{-12}

[a] Since a continuous production of TDP-43 dimers was assumed in the model, the initial concentrations of dimers become less significant over extended periods of time.

[b] A representative neuron with a soma diameter of 20 μm was considered.

[c] Mature spherical TDP-43 inclusions vary in diameter from 1 to 25 μm, while skein-like inclusions have diameters ranging from 0.5 to 1.0 μm and lengths extending up to 15 μm (Cascella et al. 2022).

[d] As there is a lack of published data on the kinetic rates in the F-W model describing the aggregation of TDP-43 protein, three representative values, 10^{-4}, 10^{-6}, 10^{-8} s^{-1}, were selected for k_1 based on information presented in Morris et al. (2008) for various proteins (summarized in Table S1). The data presented in Morris et al. (2008) were obtained by curve-fitting experimental results reported in Bieschke et al. (2005), Vestergaard et al. (2005), Lu et al. (2003), Dong et al. (2006), Zirah et al. (2006), Fink (2006), Sode et al. (2005), Chen et al. (2002), Wetzel (2006), Ban et al. (2006), Dumoulin et al. (2006), all of which are also cited in Table S1.

[e] Due to the absence of published data on the kinetic rates in the F-W model describing the aggregation of TDP-43 protein, three representative values, 10^{-4}, 10^{-6}, 10^{-8} μM^{-1} s^{-1}, were selected for k_2 based on information presented in Morris et al. (2008) for various proteins (summarized in Table S1).

[f] Given that the half-life of the first-order reaction involved in TDP-43 monomerization (refer to Eq. (1)) is on the order of hours (Oiwa et al. 2023), and the rate constant of a first-order reaction is $k_M = 0.693 / T_{1/2}$, three representative kinetic rates, 10^{-2}, 10^{-4}, 10^{-6} s^{-1}, were employed to simulate potential rates of the TDP-43 monomerization reaction.

[g] A mass of TDP-43 monomer is 43,000 dalton (Suk and Rousseaux 2020; Meneses et al. 2021; Hadley et al. 2015).

[h] Number of TDP-43 inclusion bodies is taken from Fig. 8C in Ishii et al. (2017).

[i] In cases of ALS, patients typically succumb to the disease within 2–5 years from the onset of symptoms (Prasad et al. 2019; Oiwa et al. 2023; Chhangani et al. 2021; Sugai et al. 2018). It is probable that the growth of TDP-43 inclusion bodies commenced even before the manifestation of the disease symptoms. Consequently, a growth duration of 4 years was assumed for the inclusion bodies, after which the neuron undergoes cell death.

[j] Given that the stability of TDP-43 increases in mutations (24-48 hours versus 12 hours for the wild type Prasad et al. 2019), it was hypothesized that the half-life of the misfolded form of TDP-43 is 2-4 times longer than that of the wild-type TDP-43.

[k] The reported half-life of wild-type TDP-43 is 12 hours (Ling et al. 2010; Prasad et al. 2019). Given that native TDP-43 exists in a dimeric form (Sun et al. 2014), this half-life was attributed to TDP-43 dimers.

[l] The same half-life of 12 hours was assumed for both TDP-43 monomers and TDP-43 dimers.

[m] A commonly employed density value that remains consistent across different protein types is 1.35 g/cm³ (Cavicchi et al. 2018).

2.2. Approximate analytical solution for the scenario when $T_{1/2,D} \to \infty$, $T_{1/2,M} \to \infty$, and $T_{1/2,B} \to \infty$

The approximate analytical solution is derived for a scenario where the protein degradation machinery is impaired, resulting in infinitely long half-lives for TDP-43 dimers, monomers, and aggregates. Assuming that the concentration of TDP-43 dimers is at steady state, the solution to Eq. (4) is as follows:

$$[D] = \frac{1}{k_M} \frac{q_D}{V_{soma}} a_{21} . \tag{8}$$

Adding Eqs. (5) and (6) yields the following result:

$$\frac{d[M]}{dt} + \frac{d[B]}{dt} = 2 \frac{q_D}{V_{soma}} a_{21} . \tag{9}$$

Integrating Eq. (9) yields the following result:

$$[M] + [B] = 2 \frac{q_D}{V_{soma}} a_{21} t . \tag{10}$$

The increase in $[M]+[B]$ over time is attributed to the continuous conversion of dimers into monomers.

Examining the numerical solution of Eqs. (4)-(6) reveals that $[M] \to 0$ as $t \to \infty$. Substituting this into Eq. (10) reveals that the concentration of TDP-43 aggregates can be approximated with the following equation:

$$[B] = 2 \frac{q_D}{V_{soma}} a_{21} t . \tag{11}$$

Substituting Eq. (11) into Eq. (6) results in:

$$[M] = \frac{2 \frac{q_D}{V_{soma}} a_{21}}{k_1 + k_2 2 \frac{q_D}{V_{soma}} a_{21} t} . \tag{12}$$

The approximate solution is provided by Eqs. (8), (11), and (12). It is important to recognize the utility of these equations over extended durations. However, they become invalid when $t \to 0$; for example, Eq. (12) yields $[M] = \frac{2}{k_1} \frac{q_D}{V_{soma}} a_{21}$, contradicting the initial condition given by Eq. (7b).

2.3. Size estimation for the inclusion body

The calculation of the inclusion body growth (see Fig. 1) is conducted as follows. The number of TDP-43 monomers incorporated into a single inclusion body at any given time *t* is determined according to the following equation (Watzky et al. 2008):

$$N_{single}(t) = \frac{1}{N_{IB}} \frac{[B](t)}{a_{21}} V_{soma} N_A . \tag{13}$$

Here, N_{IB} represents the number of inclusion bodies in the soma, with the assumption that all inclusion bodies have equal volumes.

Alternatively, $N_{single}(t)$ can be calculated as follows (Watzky et al. 2008):

$$N_{single}(t) = \frac{V_{single}(t)\rho_{IB}}{MW} N_A , \tag{14}$$

where MW denotes the molecular weight of TDP-43 monomers, which is the sum of the weights of all the atoms within the monomer.

By equating the expressions on the right-hand sides of Eqs. (13) and (14) and solving for the volume of a single inclusion body, the following result is obtained:

$$V_{single}(t) = \frac{[B](t)}{a_{21} N_{IB}} V_{soma} \frac{MW}{\rho_{IB}} . \tag{15}$$

Substituting Eq. (11) into Eq. (15) yields:

$$V_{single}(t) = \frac{2}{N_{IB}} \frac{MW}{\rho_{IB}} q_D t . \tag{16}$$

This implies that the volume of a single inclusion body in the soma increases linearly with both the rate of TDP-43 dimer generation and time.

TDP-43 inclusions within the soma can take on various shapes, ranging from skein-like to rounded (Cascella et al. 2022). To simplify the calculations, it was assumed that all inclusion bodies are spherical and of the same size. The volume of a spherical inclusion body can be calculated as follows:

$$V_{single}(t) = \frac{4}{3} \pi r_{IB}^3 (t) . \tag{17}$$

If the right-hand sides of Eqs. (15) and (17) are equated, and the resulting equation is solved for the radius of the inclusion body, the following result is obtained:

$$r_{IB} = \left(\frac{3}{4\pi} \frac{[B]}{a_{21} N_{IB}} V_{soma} \frac{MW}{\rho_{IB}} \right)^{1/3} . \tag{18}$$

Substituting the approximate solution (11) into Eq. (18) results in:

$$r_{IB} = \left(\frac{3}{2\pi} \frac{q_D}{N_{IB}} \frac{MW}{\rho_{IB}} \right)^{1/3} t^{1/3} . \tag{19}$$

Eq. (19) can be utilized to estimate the rate at which TDP-43 dimers are generated in the soma. If, after the growth period $t_{IB,f}$ the inclusion body's radius attains the size $r_{IB,f}$, then, according to Eq. (19), q_D can be determined as:

$$q_D = \frac{2\pi}{3} \frac{\rho_{IB}}{MW} \frac{N_{IB}}{t_{IB,f}} r_{IB,f}^3 . \tag{20}$$

2.4. Sensitivity of the inclusion body's radius to model parameters

The study investigated the sensitivity of the inclusion body's radius, denoted by r_{IB}, to various parameters in Eq. (19). Local sensitivity coefficients (Beck and Arnold 1977; Zadeh and Montas 2010; Zi 2011; Kuznetsov and Kuznetsov 2019) were computed, representing the first-order partial derivatives of the observable (in this case, the inclusion body's radius) with respect to, for example, the rate of TDP-43 dimer production, q_D, denoted by $\frac{\partial r_{IB}}{\partial q_D}$. The dimensionless relative sensitivity coefficients (Zadeh and Montas 2010; Kacser et al. 1995) were determined as the ratio of the relative change in the inclusion body's radius, $\Delta r_{IB} / r_{IB}$, to the relative change in the respective parameter, in this case, $\Delta q_D / q_D$:

$$S_{q_D}^{r_{IB}} = \frac{q_D}{r_{IB}} \frac{\partial r_{IB}}{\partial q_D} = \frac{1}{3} . \tag{21}$$

Eq. (19) was employed to calculate the derivative in Eq. (21). Importantly, the result in Eq. (21) is time-independent, indicating that the sensitivity remains constant at any given time. The positive sign of $S_{q_D}^{r_{IB}}$ suggests that r_{IB} increases with an increase in q_D. Similarly,

$$S_{MW}^{r_{IB}} = \frac{MW}{r_{IB}} \frac{\partial r_{IB}}{\partial MW} = \frac{1}{3} , \tag{22}$$

$$S_{N_{IB}}^{r_{IB}} = \frac{N_{IB}}{r_{IB}} \frac{\partial r_{IB}}{\partial N_{IB}} = -\frac{1}{3} , \tag{23}$$

$$S_{\rho_{IB}}^{r_{IB}} = \frac{\rho_{IB}}{r_{IB}} \frac{\partial r_{IB}}{\partial \rho_{IB}} = -\frac{1}{3}. \tag{24}$$

At large times, the sensitivity of r_{IB} to the kinetic constants k_1, k_2, and k_M derived from the approximate analytical solution (19) is zero. Since the approximate analytical solution is only applicable for large times, the author employed the numerical solution to calculate the sensitivity of r_{IB} to the kinetic constants at smaller times. For example:

$$S_{k_1}^{r_{IB}} = \frac{k_1}{r_{IB}} \frac{\partial r_{IB}}{\partial k_1} \approx \frac{k_1}{r_{IB}} \frac{r_{IB}\left(k_1 + \Delta k_1\right) - r_{IB}\left(k_1\right)}{\Delta k_1}\Bigg|_{\text{other parmeters kept constant}}, \tag{25}$$

where $\Delta k_1 = 10^{-3} k_1$ represents the step size. The computations were conducted using various step sizes to assess whether the sensitivity coefficients remained unaffected by the variation.

2.5. Numerical solution

Eqs. (4)-(6) with initial conditions (7) were solved using a well-validated MATLAB's ODE45 solver (MATLAB R2020b, MathWorks, Natick, MA, USA). To guarantee solution accuracy, the error tolerance parameters, RelTol and AbsTol, were set to 1e-10. The convergence was established by calculating the residuals.

3. Results

Figs. 2-7 display the radius of a TDP-43 inclusion body in a scenario where the soma contains two inclusion bodies of equal size. The model predicts the concentration of TDP-43 aggregates, which are deposited into the inclusion bodies, leading to their growth. To simplify interpretation, both inclusion bodies are assumed to be spherical, allowing the total volume of TDP-43 aggregates to be recalculated into radii for two identical spherical inclusion bodies.

Among all the model parameters listed in Table 2, the author had the least certainty regarding the values of the kinetic constants k_1, k_2, and k_M. Consequently, an investigation was conducted to evaluate the consistency of the model predictions, specifically examining the direct proportionality of the TDP-43 inclusion body radius to the cube root of time, as indicated in Eq. (19), when varying the values of the kinetic constants over a wide range.

Figs. 2-4 are calculated for the scenario of dysfunctional protein degradation machinery $T_{1/2,D} \to \infty$, $T_{1/2,M} \to \infty$, and $T_{1/2,B} \to \infty$. These figures show the effects of kinetic constants k_1, k_2, and k_M, respectively. Fig. 2 shows that for $t > 0.04$ years the inclusion body's radius, r_{IB}, remains unaffected by the kinetic constant, k_1, that governs the conversion of TDP-43 monomers into a misfolded, aggregating form by nucleation. This is consistent with the approximate solution given by Eq. (19), indicating that the radius is insensitive to the kinetic constants. However, the validity of the approximate solution is limited to extended timeframes (for the parameter values used in computing Fig. 2, it is $t > 0.04$ years). Fig. 2 shows that numerical solutions for $t > 0.04$ years precisely agree with the approximate solution given by Eq. (19), indicating that the inclusion body's radius grows directly in proportion to $t^{1/3}$.

The concentrations of TDP-43 dimers, monomers, and aggregates are plotted in the Supplemental Materials. The concentration of dimers, [*D*], quickly stabilizes (in less than 0.002 years) at a constant value, determined by the balance of dimer production and dimer conversion into monomers (Fig. S1).

As monomers convert into aggregates, the concentration of monomers, [*M*], decreases over time, initially rapidly and then gradually (Fig. S2). The numerical and analytical solutions converge at large times, but the time it takes for the solutions to align depends on the value of k_1. The convergence is slower for larger values of k_1, taking approximately one year for the numerical solution to match the approximate solution when $k_1 = 10^{-4}$ s^{-1}.

The approximate solution indicates a linear increase in the concentration of aggregates over time, with numerical and analytical solutions converging in approximately 0.04 hours (Fig. S3). It is important to note that the plotted TDP-43 aggregate concentration does not yet account for the removal of aggregates from the cytosol due to their deposition into inclusion bodies. The model simulating the growth of the inclusion body radius assumes that all aggregates are eventually deposited into inclusion bodies, see Eq. (18).

For various values of k_2, describing the rate of autocatalytic aggregation of TDP-43 monomers, the numerical solution for the inclusion body's radius, r_{IB}, also converges to the approximate solution given by Eq. (19). The convergence rate depends on k_2, with the slowest convergence observed for the smallest tested value, $k_2 = 10^{-8}$ μM^{-1} s^{-1}. In this case, it takes approximately 0.4 years for the numerical solution to converge to the approximate solution (Fig. 3). The concentrations of TDP-43 dimers, monomers, and aggregates also quickly converge to those given by the approximate solution (Figs. S4-S6). Notably, the

concentration of aggregates reaches a linearly increasing curve with time (Fig. S6), attributed to the constant supply of TDP-43 dimers at a rate of q_D.

Testing the numerical solution for various values of k_M, representing the rate of conversion of TDP-43 dimers into monomers, revealed that the numerical solution for r_{IB} converges to the cube root of time dependence, as predicted by the approximate solution in Eq. (19). The rate of convergence depends on the value of k_M (see Fig. 4), with the slowest convergence observed for the smallest tested value of 10^{-6} s^{-1}. The concentration of TDP-43 dimers, [*D*] (Fig. S7), is influenced by k_M, as it is inversely proportional to k_M for a constant value of q_D (see Eq. (8)). Numerical solutions converge to the approximate analytical solutions predicted by Eq. (8), resulting in three distinct curves corresponding to different values of k_M (Fig. S7). Conversely, the concentrations of monomers, [*M*], and aggregates, [*B*], converge to the same analytical solution independent of the value of k_M (Figs. S8 and S9).

Figs. 5-7 are computed for physiologically relevant half-lives of TDP-43 dimers, monomers, and aggregates ($T_{1/2,D} = 4.32\times10^4$ s, $T_{1/2,M} = 4.32\times10^4$ s, and $T_{1/2,B} = 1.30\times10^5$ s). These figures show the effects of kinetic constants k_1, k_2, and k_M, respectively. The approximate solution is not plotted, as it is exclusively applicable to the scenario involving infinite half-lives of TDP-43 dimers, monomers, and aggregates. In contrast to the situation with infinite half-lives, the curves depicting the radii of inclusion bodies do not converge to the curve displaying a cube root of time as time increases. For different values of kinetic constants (k_1, k_2, and k_M), the curves representing r_{IB} converge to different constant values determined by the production of TDP-43 aggregates and their degradation due to their finite half-life.

The concentration of TDP-43 dimers, [*D*], is independent of kinetic constants k_1 and k_2 (Figs. S10 and S13), but depends on the value of k_M (Fig. S16). The concentration of TDP-43 monomers, [*M*], depends on the values of k_1, k_2, and k_M (Figs. S11, S14, and S17). The concentration of TDP-43 aggregates, [*B*], depends on the values of k_1, k_2, and k_M (Figs. S12, S15, and S18).

Fig. 8 explores the sensitivity of the inclusion body's radius, r_{IB}, to the kinetic constants k_1, k_2, and k_M for the scenario with infinite half-life of TDP-43 dimers, monomers, and aggregates. The sensitivity is positive at small times and, at large times, it converges toward the limiting value of zero, consistent with the approximate analytical solution (19).

4. Discussion, limitations of the model, and future directions

This paper has formulated a model for the growth of TDP-43 inclusion bodies. The model predicts the concentrations of TDP-43 dimers, monomers, and aggregates while operating under the assumption that all aggregates integrate into the inclusion bodies.

In the case of dysfunctional protein degradation machinery, leading to infinite half-lives of protein dimers, monomers, and aggregates, the model predicts that the inclusion body's radius increases in proportion to the cube root of time. As kinetic constants governing the rates of TDP-43 monomerization, nucleation, and autocatalytic growth are undocumented in the literature, an investigation was conducted to determine the consistency of model predictions across a wide range of values for these kinetic constants. The findings revealed that model predictions are influenced by the kinetic constants only at small times. The derived approximate solution, valid for large times, demonstrates that the concentrations of TDP-43 monomers and aggregates and the radius of the inclusion body remain unaffected by the kinetic constants. The approximate solution indicates a linear increase in aggregate concentration over time, attributed to the continuous synthesis of TDP-43 dimers in the cytoplasm.

The approximate solution becomes invalid for the scenario with physiologically relevant half-lives of TDP-43 dimers, monomers, and aggregates. Unlike the situation with infinite half-lives, the curves depicting the radii of inclusion bodies do not converge to the curve displaying a cube root of time as time increases. For various values of kinetic constants, the curves representing concentrations of monomers and aggregates, as well as the curves depicting the inclusion body radii, converge to distinct constant values.

For infinite half-lives of TDP-43 dimers, monomers, and aggregates, the sensitivity of the inclusion body's radius to the kinetic constants is positive at small times and, at large times, it converges toward the limiting value of zero. This indicates that at large times, the inclusion body's radius becomes independent of the kinetic constants.

The analysis presented here has limitations, primarily due to its reliance on a simplified mechanism of TDP-43 cytoplasmic mislocalization and subsequent aggregation, compounded by the absence of precise values for kinetic constants.

Future studies should concentrate on developing more precise models for TDP-43 oligomerization, covering the entire spectrum of oligomeric species, including trimers, tetramers, and multimers. Furthermore, it is necessary to integrate the processes of TDP-43 phosphorylation and ubiquitination into these models. Investigating the potential prion-like spread of pathological TDP-43 species is also a crucial

avenue for future exploration. Comparing model predictions with future experimental data will be crucial to provide quantitative evidence either supporting or challenging the developed theory.

Incorporating modern mathematical techniques designed for biological problems, particularly those that provide tools for accounting for the elasticity of domain (in this case – neuron) boundaries, would greatly enhance future models (Alghamdi et al. 2024; Sher Akbar et al. 2023; Maraj et al. 2023; Ghailan et al. 2023; Akbar et al. 2023; Akram and Akbar 2023; Akbar and Muhammad 2023; Akbar et al. 2024; Noreen and Akhtar 2023).

Acknowledgment

The author acknowledges the support provided by the National Science Foundation (grant CBET-2042834) and the Alexander von Humboldt Foundation through the Humboldt Research Award.

References

Akbar NS, Akhtar S, Maraj EN, Anqi AE, Homod RZ. 2023. Heat transfer analysis of MHD viscous fluid in a ciliated tube with entropy generation. Mathematical Methods in the Applied Sciences. 46:11495-11508.

Akbar NS, Muhammad T. 2023. Physical aspects of electro osmotically interactive cilia propulsion on symmetric plus asymmetric conduit flow of couple stress fluid with thermal radiation and heat transfer. Scientific Reports. 13:18491.

Akbar NS, Rafiq M, Muhammad T, Alghamdi M. 2024. Electro osmotically interactive biological study of thermally stratified micropolar nanofluid flow for copper and silver nanoparticles in a microchannel. Scientific Reports. 14:518.

Akram J, Akbar NS. 2023. Electroosmotically actuated peristaltic-ciliary flow of propylene glycol + water conveying titania nanoparticles. Scientific Reports. 13:11801.

Alghamdi M, Akbar NS, Zamir T, Muhammad T. 2024. Double layered combined convective heated flow of eyring-powell fluid across an elevated stretched cylinder using intelligent computing approach. Case Studies in Thermal Engineering. 54:104009.

Ban T, Yamaguchi K, Goto Y. 2006. Direct observation of amyloid fibril growth, propagation, and adaptation. Accounts of Chemical Research. 39:663-670.

Beck JV, Arnold KJ. 1977. Parameter estimation in science and engineering. New York: Wiley.

Bieschke J, Zhang Q, Powers ET, Lerner RA, Kelly JW. 2005. Oxidative metabolites accelerate Alzheimer's amyloidogenesis by a two-step mechanism, eliminating the requirement for nucleation. Biochemistry. 44:4977-4983.

Capitini C, Conti S, Perni M, Guidi F, Cascella R, De Poli A, Penco A, Relini A, Cecchi C, Chiti F. 2014. TDP-43 inclusion bodies formed in bacteria are structurally amorphous, non-amyloid and inherently toxic to neuroblastoma cells. PLOS One. 9:e86720.

Cascella R, Bigi A, Riffert DG, Gagliani MC, Ermini E, Moretti M, Cortese K, Cecchi C, Chiti F. 2022. A quantitative biology approach correlates neuronal toxicity with the largest inclusions of TDP-43. Science Advances. 8:eabm6376.

Cavicchi RE, King J, Ripple DC. 2018. Measurement of average aggregate density by sedimentation and brownian motion analysis. Journal of Pharmaceutical Sciences. 107:1304-1312.

Chen S, Ferrone FA, Wetzel R. 2002. Huntington's disease age-of-onset linked to polyglutamine aggregation nucleation. Proceedings of the National Academy of Sciences of the United States of America. 99:11884-11889.

Chhangani D, Martín-Peña A, Rincon-Limas DE. 2021. Molecular, functional, and pathological aspects of TDP-43 fragmentation. iScience. 24:102459.

Chong PA, Forman-Kay J. 2016. A new phase in ALS research. Structure. 24:1435-1436.

Dong J, Shokes JE, Scott RA, Lynn DG. 2006. Modulating amyloid self-assembly and fibril morphology with Zn(II). Journal of the American Chemical Society. 128:3540-3542.

Dumoulin M, Kumita JR, Dobson CM. 2006. Normal and aberrant biological self-assembly: Insights from studies of human lysozyme and its amyloidogenic variants. Accounts of Chemical Research. 39:603-610.

Fink AL. 2006. The aggregation and fibrillation of alpha-synuclein. Accounts of Chemical Research. 39:628-634.

Finke RG, Watzky MA, Whitehead CB. 2020. Response to "Particle size is a primary determinant for sigmoidal kinetics of nanoparticle formation: A "Disproof" of the Finke–Watzky (F-W) nanoparticle nucleation and growth mechanism". Chemistry of Materials. 32:3657-3672.

French RL, Grese ZR, Aligireddy H, Dhavale DD, Reeb AN, Kedia N, Kotzbauer PT, Bieschke J, Ayala YM. 2019. Detection of TAR DNA-binding protein 43 (TDP-43) oligomers as initial intermediate species during aggregate formation. The Journal of Biological Chemistry. 294:6696-6709.

Ghailan KY, Akbar NS, Albakri A, Alshehri MM. 2023. Biological analysis of emerging nanoparticles with blood through propagating flow along a plumb porous canal in the occurrence of energy and heat transfer. Surfaces and Interfaces. 40:103013.

Glass JD. 2020. Stathmin-2: Adding another piece to the puzzle of TDP-43 proteinopathies and neurodegeneration. The Journal of Clinical Investigation. 130:5677-5680.

Grossman M, Seeley WW, Boxer AL, Hillis AE, Knopman DS, Ljubenov PA, Miller B, Piguet O, Rademakers R, Whitwell JL, Zetterberg H, van Swieten JC. 2023. Frontotemporal lobar degeneration. Nature Reviews Disease Primers. 9:40.

Hadley KC, Rakhit R, Guo H, Sun Y, Jonkman JEN, McLaurin J, Hazrati L, Emili A, Chakrabartty A. 2015. Determining composition of micron-scale protein deposits in neurodegenerative disease by spatially targeted optical microproteomics. eLife. 4:e09579.

Iashchishyn IA, Sulskis D, Nguyen Ngoc M, Smirnovas V, Morozova-Roche LA. 2017. Finke-Watzky two-step nucleation-autocatalysis model of S100A9 amyloid formation: Protein misfolding as "nucleation" event. ACS Chemical Neuroscience. 8:2152-2158.

Ishii T, Kawakami E, Endo K, Misawa H, Watabe K. 2017. Formation and spreading of TDP-43 aggregates in cultured neuronal and glial cells demonstrated by time-lapse imaging. PLOS One. 12:e0179375.

Jiang L, Xue W, Hong J, Zhang J, Li M, Yu S, He J, Hu H. 2017. The N-terminal dimerization is required for TDP-43 splicing activity. Scientific Reports. 7:6196.

Jo M, Lee S, Jeon Y, Kim S, Kwon Y, Kim H. 2020. The role of TDP-43 propagation in neurodegenerative diseases: Integrating insights from clinical and experimental studies. Experimental & Molecular Medicine. 52:1652-1662.

Kacser H, Burns JA, Fell DA. 1995. The control of flux. Biochemical Society Transactions. 23:341-366.

Kuznetsov AV. 2024a. Lewy body radius growth: The hypothesis of the cube root of time dependency. J Theor Biol. 581:111734.

Kuznetsov AV. 2024b. Numerical and analytical simulation of the growth of amyloid-β plaques. ASME Journal of Biomedical Engineering. 146:061004.

Kuznetsov IA, Kuznetsov AV. 2019. Investigating sensitivity coefficients characterizing the response of a model of tau protein transport in an axon to model parameters. Computer Methods in Biomechanics and Biomedical Engineering. 22:71-83.

Kuznetsov IA, Kuznetsov AV. 2022. An analytical solution simulating growth of Lewy bodies. Mathematical Medicine and Biology: A Journal of the IMA. 39:299-312.

Ling S, Albuquerque CP, Han JS, Lagier-Tourenne C, Tokunaga S, Zhou H, Cleveland DW. 2010. ALS-associated mutations in TDP-43 increase its stability and promote TDP-43 complexes with FUS/TLS. Proceedings of the National Academy of Sciences of the United States of America. 107:13318-13323.

Lu K, Jacob J, Thiyagarajan P, Conticello VP, Lynn DG. 2003. Exploiting amyloid fibril lamination for nanotube self-assembly. Journal of the American Chemical Society. 125:6391-6393.

Maraj EN, Shah SI, Akbar NS, Muhammad T. 2023. Thermally progressive particle-cu/blood peristaltic transport with mass transfer in a non-uniform wavy channel: Closed-form exact solutions. Alexandria Engineering Journal. 74:453-466.

Meneses A, Koga S, O'Leary J, Dickson DW, Bu G, Zhao N. 2021. TDP-43 pathology in Alzheimer's disease. Molecular Neurodegeneration. 16:84.

Morris AM, Watzky MA, Agar JN, Finke RG. 2008. Fitting neurological protein aggregation kinetic data via a 2-step, minimal/"Ockham's razor" model: The Finke-Watzky mechanism of nucleation followed by autocatalytic surface growth. Biochemistry. 47:2413-2427.

Necarsulmer, J., Simon, J., Evangelista, B., Chen, Y., Tian, X., Nafees, S., Marquez Gonzalez, A., Jiang, H., Wang, P., Ajit, D., Nikolova, V., Harper, K., Ezzell, J., Feng-Chang, Beltran, A., Moy, S., Cohen, T.: *RNA-binding deficient TDP-43 drives cognitive decline in a mouse model of TDP-43 proteinopathy* eLife Sciences Publications, Ltd. (2023)

Noreen SA, Akhtar S. 2023. Metachronal wave form analysis on cilia-driven flow of non-newtonain Phan–Thien–Tanner fluid model: A physiological mathematical model. Proceedings of the Institution of Mechanical Engineers, Part E: Journal of Process Mechanical Engineering. 237:2567-2573.

Oiwa K, Watanabe S, Onodera K, Iguchi Y, Kinoshita Y, Komine O, Sobue A, Okada Y, Katsuno M, Yamanaka K. 2023. Monomerization of TDP-43 is a key determinant for inducing TDP-43 pathology in amyotrophic lateral sclerosis. Science Advances. 9:eadf6895.

Pérez-Berlanga M, Wiersma VI, Zbinden A, De Vos L, Wagner U, Foglieni C, Mallona I, Betz KM, Cléry A, Weber J, Guo Z, Rigort R, de Rossi P, Manglunia R, Tantardini E, Sahadevan S, Stach O, Hruska-Plochan M, Allain FH, Paganetti P, Polymenidou M. 2023. Loss of TDP-43 oligomerization or RNA binding elicits distinct aggregation patterns. The EMBO Journal. 42:e111719.

Prasad A, Bharathi V, Sivalingam V, Girdhar A, Patel BK. 2019. Molecular mechanisms of TDP-43 misfolding and pathology in amyotrophic lateral sclerosis. Frontiers in Molecular Neuroscience. 12:25.

Sher Akbar N, Abouei Mehrizi A, Rafiq M, Bilal Habib M, Muhammad T. 2023. Peristaltic flow analysis of thermal engineering nano model with effective thermal conductivity of different shape nanomaterials assessing variable fluid properties. Alexandria Engineering Journal. 81:395-404.

Sode K, Usuzaka E, Kobayashi N, Ochiai S. 2005. Engineered alpha-synuclein prevents wild type and familial parkin variant fibril formation. Biochemical and Biophysical Research Communications. 335:432-436.

Sugai A, Kato T, Koyama A, Koike Y, Kasahara S, Konno T, Ishihara T, Onodera O. 2018. Robustness and vulnerability of the autoregulatory system that maintains nuclear TDP-43 levels: A trade-off hypothesis for ALS pathology based on in silico data. Frontiers in Neuroscience. 12:28.

Suk TR, Rousseaux MWC. 2020. The role of TDP-43 mislocalization in amyotrophic lateral sclerosis. Molecular Neurodegeneration. 15:45.

Sun Y, Arslan PE, Won A, Yip CM, Chakrabartty A. 2014. Binding of TDP-43 to the 3′UTR of its cognate mRNA enhances its solubility. Biochemistry. 53:5885-5894.

Sun Y, Medina Cruz A, Hadley KC, Galant NJ, Law R, Vernon RM, Morris VK, Robertson J, Chakrabartty A. 2019. Physiologically important electrolytes as regulators of TDP-43 aggregation and droplet-phase behavior. Biochemistry. 58:590-607.

Vestergaard M, Kerman K, Saito M, Nagatani N, Takamura Y, Tamiya E. 2005. A rapid label-free electrochemical detection and kinetic study of Alzheimer's amyloid beta aggregation. Journal of the American Chemical Society. 127:11892-11893.

Watzky MA, Finney EE, Finke RG. 2008. Transition-metal nanocluster size vs formation time and the catalytically effective nucleus number: A mechanism-based treatment. Journal of the American Chemical Society. 130:11959-11969.

Wetzel R. 2006. Kinetics and thermodynamics of amyloid fibril assembly. Accounts of Chemical Research. 39:671-679.

Zadeh KS, Montas HJ. 2010. A class of exact solutions for biomacromolecule diffusion-reaction in live cells. Journal of Theoretical Biology. 264:914-933.

Zi Z. 2011. Sensitivity analysis approaches applied to systems biology models. Iet Systems Biology. 5:336-346.

Zirah S, Kozin SA, Mazur AK, Blond A, Cheminant M, Ségalas-Milazzo I, Debey P, Rebuffat S. 2006. Structural changes of region 1-16 of the Alzheimer disease amyloid beta-peptide upon zinc binding and in vitro aging. The Journal of Biological Chemistry. 281:2151-2161.

Figure captions

Fig. 1. A diagram depicting a neuron with two TDP-43 inclusion bodies of equal size located in the soma. The inclusion bodies shown in Fig. 1 are not drawn to scale. *Figure generated with the aid of servier medical art, licensed under a creative commons attribution 3.0 generic license. http://Smart.servier.com.*

Fig. 2. (a) The radius of the growing inclusion body vs time (in years). The results are displayed for three values of k_1. The model predicts the total volume of all inclusion bodies in the soma as $N_{IB}V_{single}$. Assuming all inclusion bodies have the same volume, the total volume is recalculated into the volume of a single inclusion body, denoted by V_{single} (Eqs. (15) and (16)). The predicted volume is converted into the radius of a sphere with an equivalent volume to facilitate interpretation. (b) Similar to Fig. 2a, but concentrating on a specific time range of [0 0.04 year]. The concentration of the misfolded form of TDP-43, [*B*], is obtained by numerically solving Eqs. (4)-(6) with the initial condition (7), and the radius of the inclusion body is calculated by using Eq. (18). The approximate solution is determined by employing Eq. (19). The presented scenario assumes dysfunctional protein degradation machinery with $T_{1/2,D} \to \infty$, $T_{1/2,M} \to \infty$, and $T_{1/2,B} \to \infty$. $k_2 = 10^{-6}$ μM^{-1} s^{-1} and $k_M = 10^{-4}$ s^{-1}.

Fig. 3. (a) The radius of the growing inclusion body vs time (in years). The results are displayed for three values of k_2. (b) Similar to Fig. 3a but concentrating on a specific time range of [0 0.4 year]. The approximate solution is determined by employing Eq. (19). The presented scenario assumes dysfunctional protein degradation machinery with $T_{1/2,D} \to \infty$, $T_{1/2,M} \to \infty$, and $T_{1/2,B} \to \infty$. $k_1 = 10^{-6}$ s^{-1} and $k_M = 10^{-4}$ s^{-1}.

Fig. 4. (a) The radius of the growing inclusion body vs time (in years). The results are displayed for three values of k_M. (b) Similar to Fig. 4a but concentrating on a specific time range of [0 1 year]. The approximate solution is determined by employing Eq. (19). The presented scenario assumes dysfunctional protein degradation machinery with $T_{1/2,D} \to \infty$, $T_{1/2,M} \to \infty$, and $T_{1/2,B} \to \infty$. $k_1 = 10^{-6}$ s^{-1} and $k_2 = 10^{-6}$ μM^{-1} s^{-1}.

Fig. 5. (a) The radius of the growing inclusion body vs time (in years). The results are displayed for three values of k_1. (b) Similar to Fig. 5a but concentrating on a specific time range of [0 0.04 year]. The presented scenario assumes physiologically relevant values for the half-lives of TDP-43 dimers, monomers, and aggregates. $T_{1/2,D} = 4.32 \times 10^4$ s, $T_{1/2,M} = 4.32 \times 10^4$ s, and $T_{1/2,B} = 1.30 \times 10^5$ s. The

approximate solution is not displayed as it applies exclusively to the scenario involving infinite half-lives of TDP-43 dimers, monomers, and aggregates. $k_2 = 10^{-6}$ μM^{-1} s^{-1} and $k_M = 10^{-4}$ s^{-1}.

Fig. 6. (a) The radius of the growing inclusion body vs time (in years). The results are displayed for three values of k_2. (b) Similar to Fig. 6a but concentrating on a specific time range of [0 0.04 year]. The presented scenario assumes physiologically relevant values for the half-lives of TDP-43 dimers, monomers, and aggregates. $T_{1/2,D} = 4.32 \times 10^4$ s, $T_{1/2,M} = 4.32 \times 10^4$ s, and $T_{1/2,B} = 1.30 \times 10^5$ s. The approximate solution is not displayed as it applies exclusively to the scenario involving infinite half-lives of TDP-43 dimers, monomers, and aggregates. $k_1 = 10^{-6}$ s^{-1} and $k_M = 10^{-4}$ s^{-1}.

Fig. 7. (a) The radius of the growing inclusion body vs time (in years). The results are displayed for three values of k_M. (b) Similar to Fig. 7a but concentrating on a specific time range of [0 0.04 year]. The presented scenario assumes physiologically relevant values for the half-lives of TDP-43 dimers, monomers, and aggregates. $T_{1/2,D} = 4.32 \times 10^4$ s, $T_{1/2,M} = 4.32 \times 10^4$ s, and $T_{1/2,B} = 1.30 \times 10^5$ s. The approximate solution is not displayed as it applies exclusively to the scenario involving infinite half-lives of TDP-43 dimers, monomers, and aggregates. $k_1 = 10^{-6}$ s^{-1} and $k_2 = 10^{-6}$ μM^{-1} s^{-1}.

Fig. 8. The dimensionless sensitivity of the inclusion body's radius, r_{IB}, to:

(a) the rate constant linked to the first pseudoelementary step in the F-W model, describing aggregate formation through nucleation, k_1 (calculated for $k_2 = 10^{-6}$ μM^{-1} s^{-1}, $k_M = 10^{-4}$ s^{-1} for three distinct values of k_1);

(b) the rate constant associated with the second pseudoelementary step in the F-W model, describing aggregate formation through autocatalytic growth, k_2 (calculated for $k_1 = 10^{-6}$ s^{-1}, $k_M = 10^{-4}$ s^{-1} for three distinct values of k_2);

(c) the rate constant linked to the reaction describing the conversion of TDP-43 dimers into monomers, k_M (calculated for $k_1 = 10^{-6}$ s^{-1}, $k_2 = 10^{-6}$ μM^{-1} s^{-1} for three distinct values of k_M).

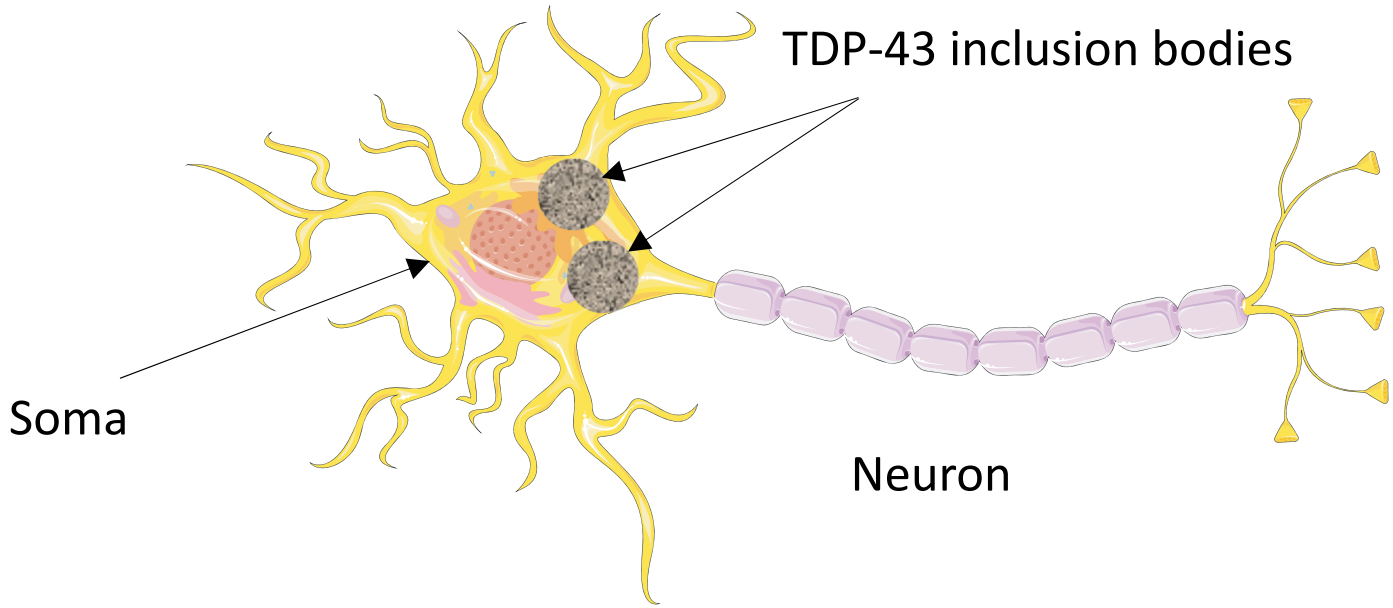

Figure 1

(a)

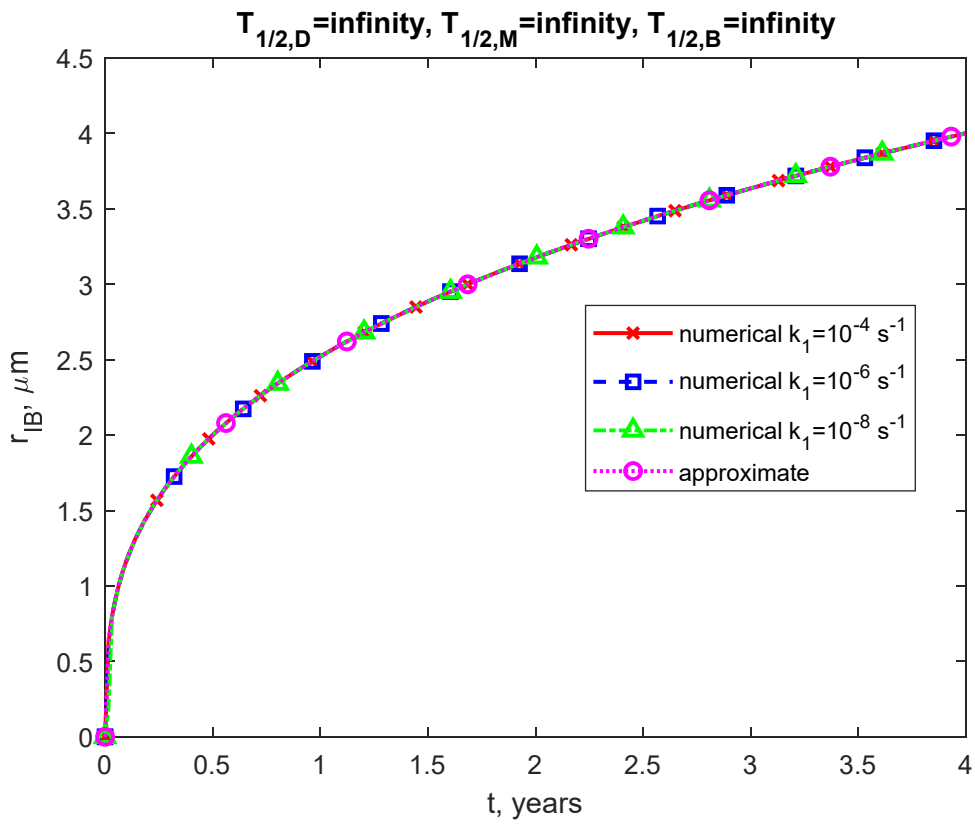
T1/2,D=infinity, T1/2,M=infinity, T1/2,B=infinity
rIB, μm
t, years
numerical k1=10-4 s-1
numerical k1=10-6 s-1
numerical k1=10-8 s-1
approximate

(b)

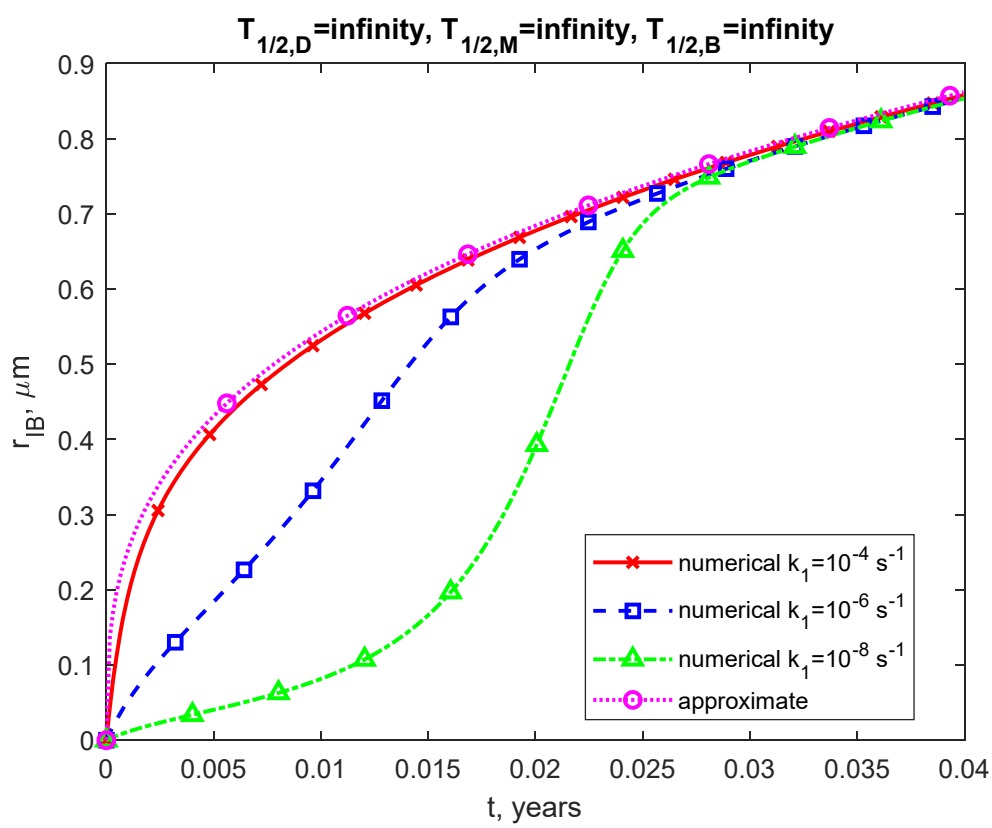
T1/2,D=infinity, T1/2,M=infinity, T1/2,B=infinity
rIB, μm
t, years
numerical k1=10-4 s-1
numerical k1=10-6 s-1
numerical k1=10-8 s-1
approximate

Figure 2

(a)

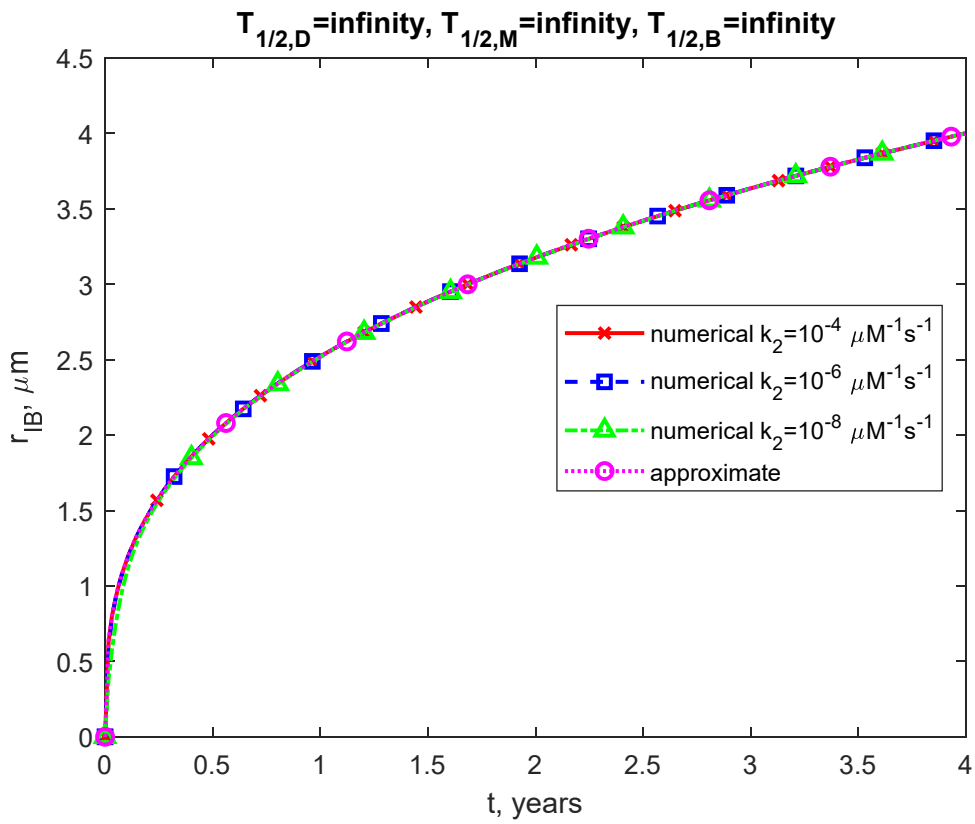
T1/2,D=infinity, T1/2,M=infinity, T1/2,B=infinity
rIB, μm
t, years
numerical k2=10-4 μM-1s-1
numerical k2=10-6 μM-1s-1
numerical k2=10-8 μM-1s-1
approximate

(b)

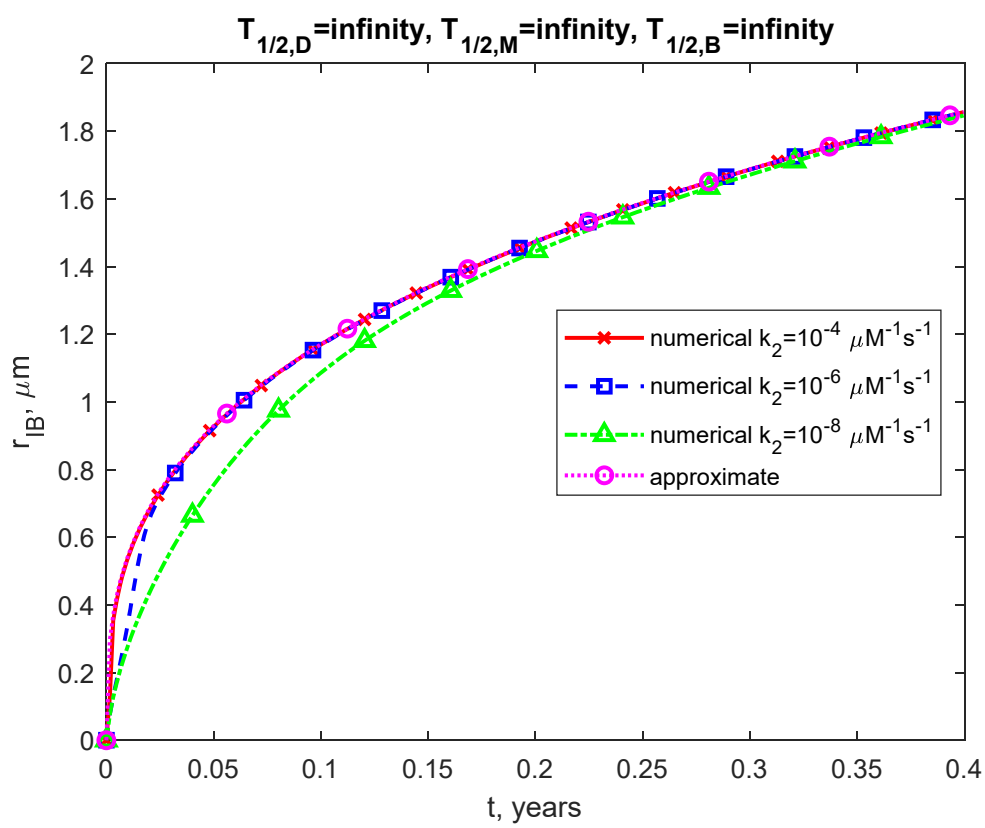
T1/2,D=infinity, T1/2,M=infinity, T1/2,B=infinity
rIB, μm
t, years
numerical k2=10-4 μM-1s-1
numerical k2=10-6 μM-1s-1
numerical k2=10-8 μM-1s-1
approximate

Figure 3

(a)

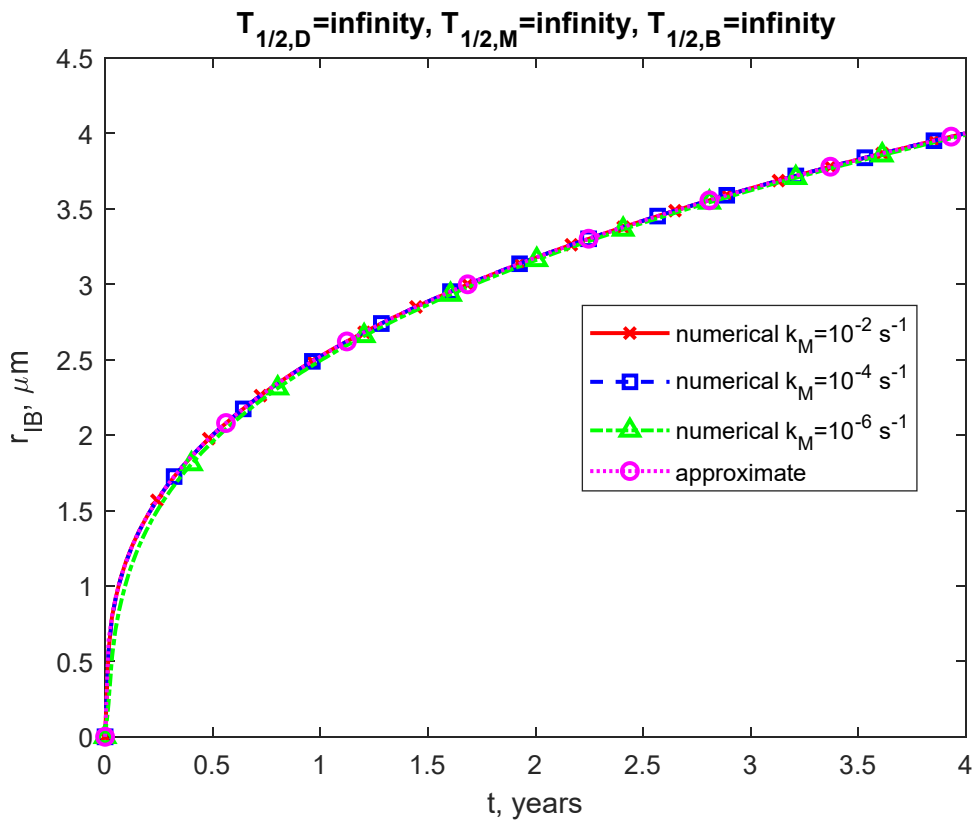
T 1/2,D=infinity, T 1/2,M=infinity, T 1/2,B=infinity
r IB, μm
t, years
numerical k M=10-2 s-1
numerical k M=10-4 s-1
numerical k M=10-6 s-1
approximate

(b)

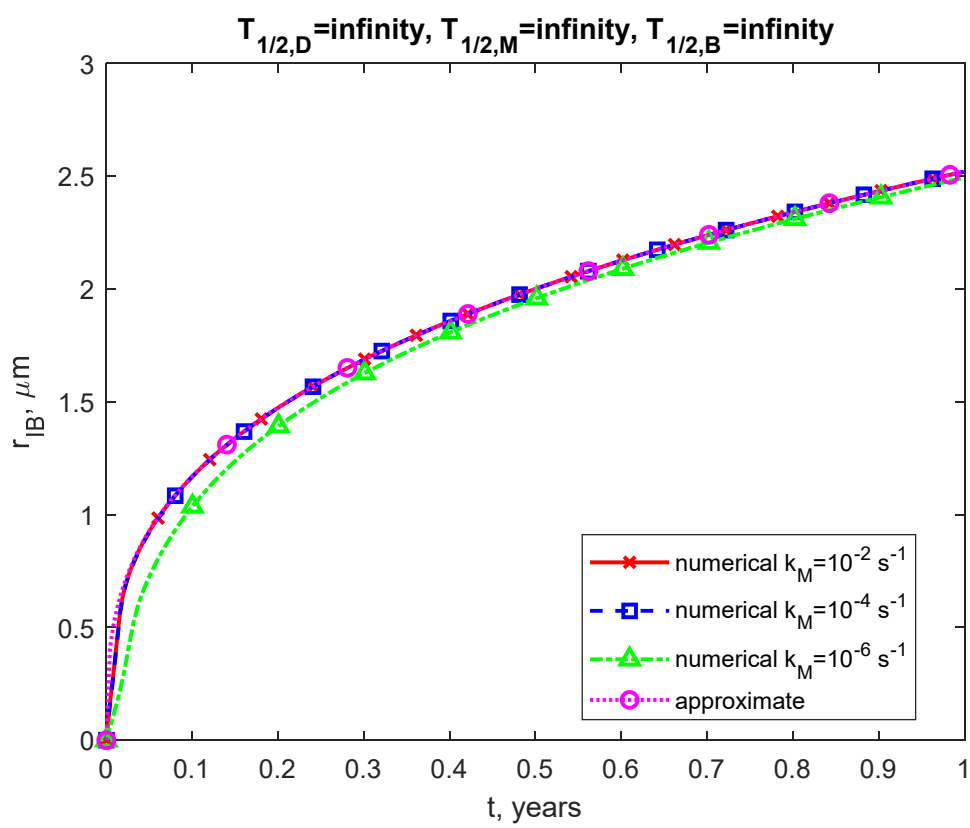
T 1/2,D=infinity, T 1/2,M=infinity, T 1/2,B=infinity
r IB, μm
t, years
numerical k M=10-2 s-1
numerical k M=10-4 s-1
numerical k M=10-6 s-1
approximate

Figure 4

(a)

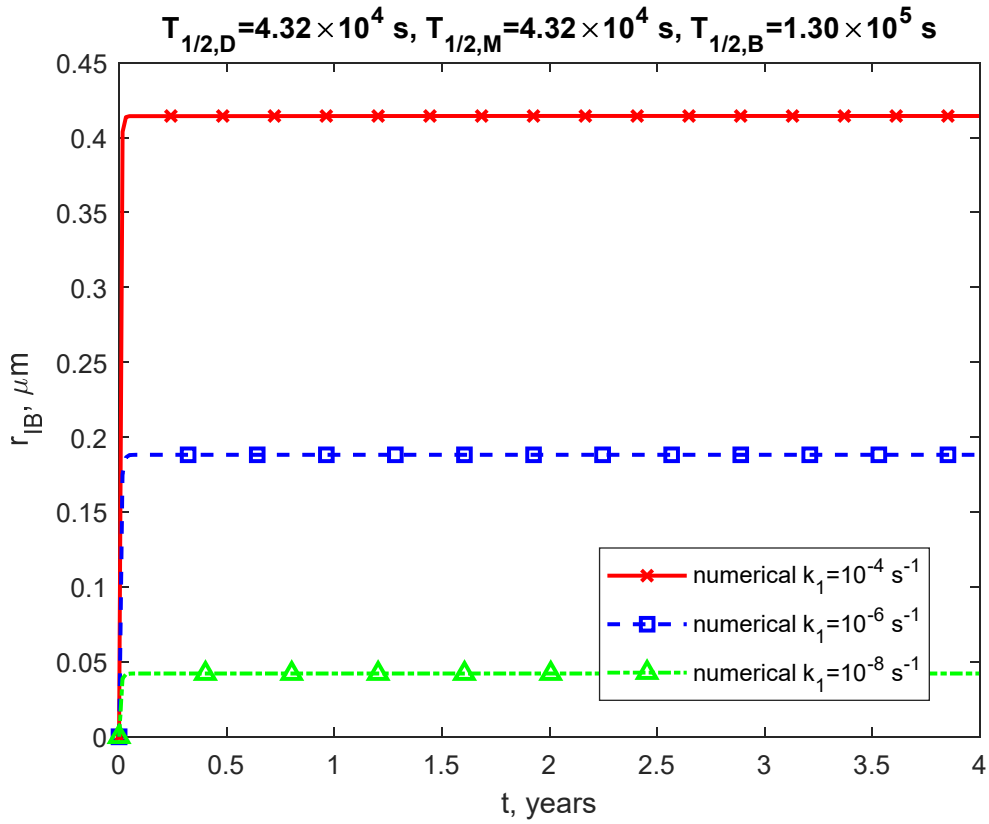
$T_{1/2,D}$=4.32×10^4 s, $T_{1/2,M}$=4.32×10^4 s, $T_{1/2,B}$=1.30×10^5 s
r_{IB}, μm
t, years
numerical k_1=10^-4 s^-1
numerical k_1=10^-6 s^-1
numerical k_1=10^-8 s^-1

(b)

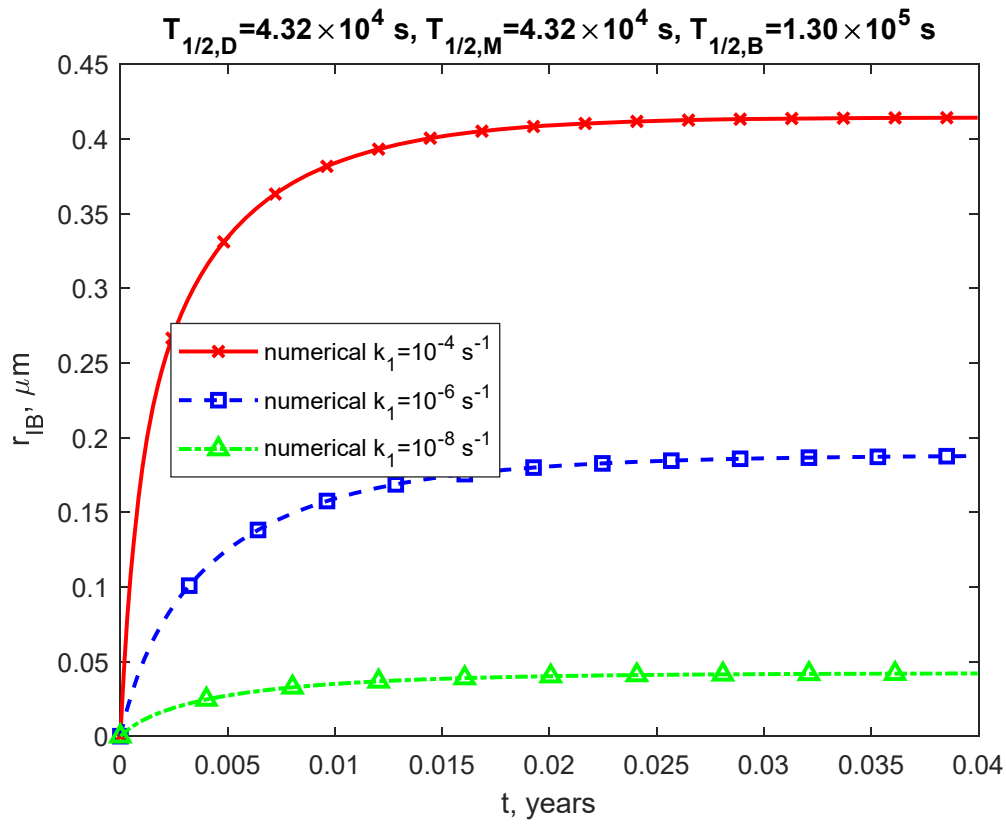
$T_{1/2,D}$=4.32×10^4 s, $T_{1/2,M}$=4.32×10^4 s, $T_{1/2,B}$=1.30×10^5 s
r_{IB}, μm
t, years
numerical k_1=10^-4 s^-1
numerical k_1=10^-6 s^-1
numerical k_1=10^-8 s^-1

Figure 5

(a)

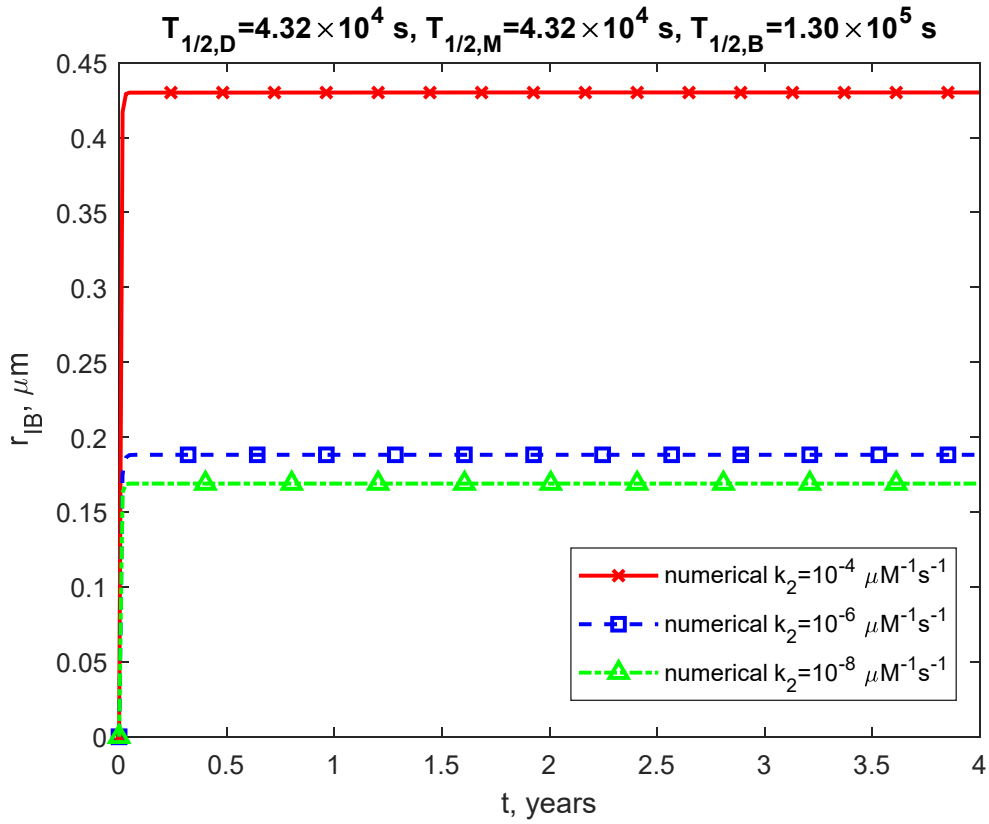
$T_{1/2,D}$=4.32×10^4 s, $T_{1/2,M}$=4.32×10^4 s, $T_{1/2,B}$=1.30×10^5 s
r_{IB}, μm
t, years
numerical k_2=10^-4 μM^-1s^-1
numerical k_2=10^-6 μM^-1s^-1
numerical k_2=10^-8 μM^-1s^-1

(b)

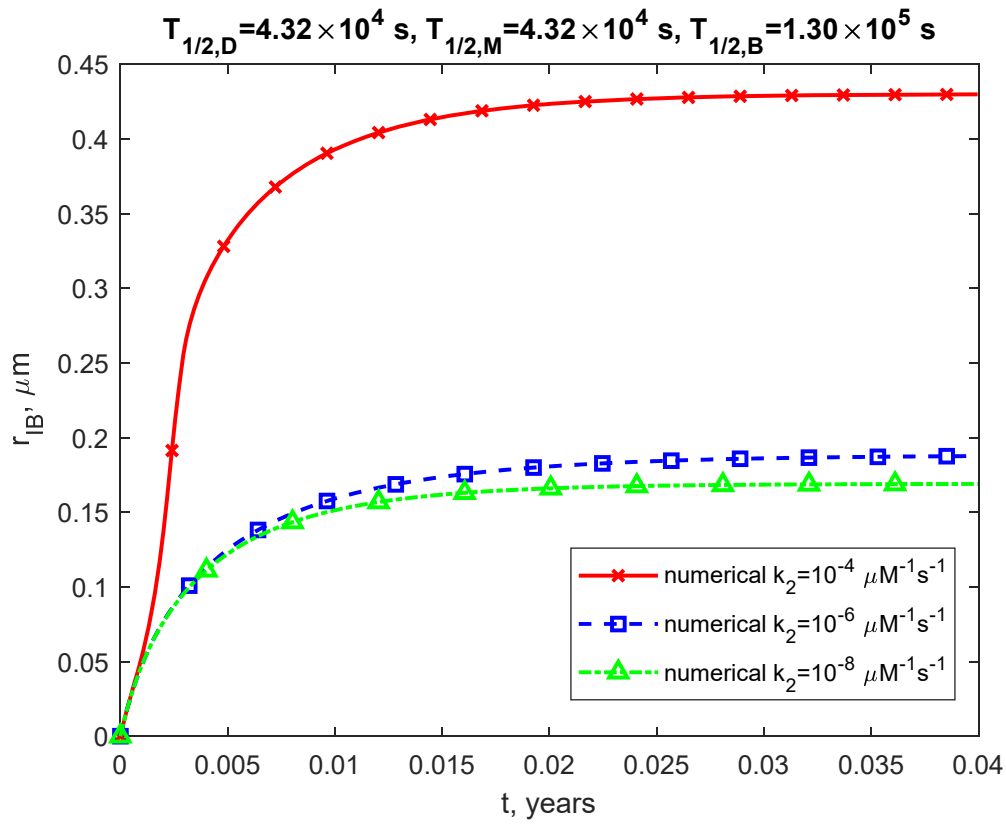
$T_{1/2,D}$=4.32×10^4 s, $T_{1/2,M}$=4.32×10^4 s, $T_{1/2,B}$=1.30×10^5 s
r_{IB}, μm
t, years
numerical k_2=10^-4 μM^-1s^-1
numerical k_2=10^-6 μM^-1s^-1
numerical k_2=10^-8 μM^-1s^-1

Figure 6

(a)

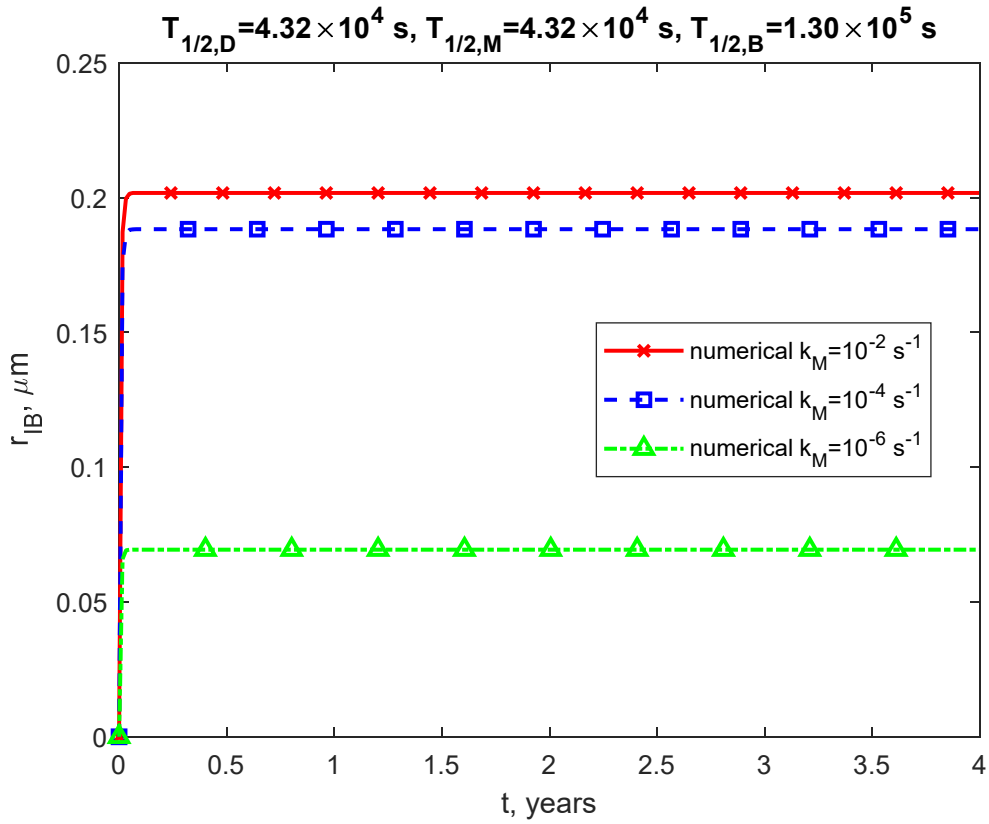
$T_{1/2,D}$=4.32×10^4 s, $T_{1/2,M}$=4.32×10^4 s, $T_{1/2,B}$=1.30×10^5 s
r_{IB}, μm
t, years
numerical k_M=10^-2 s^-1
numerical k_M=10^-4 s^-1
numerical k_M=10^-6 s^-1

(b)

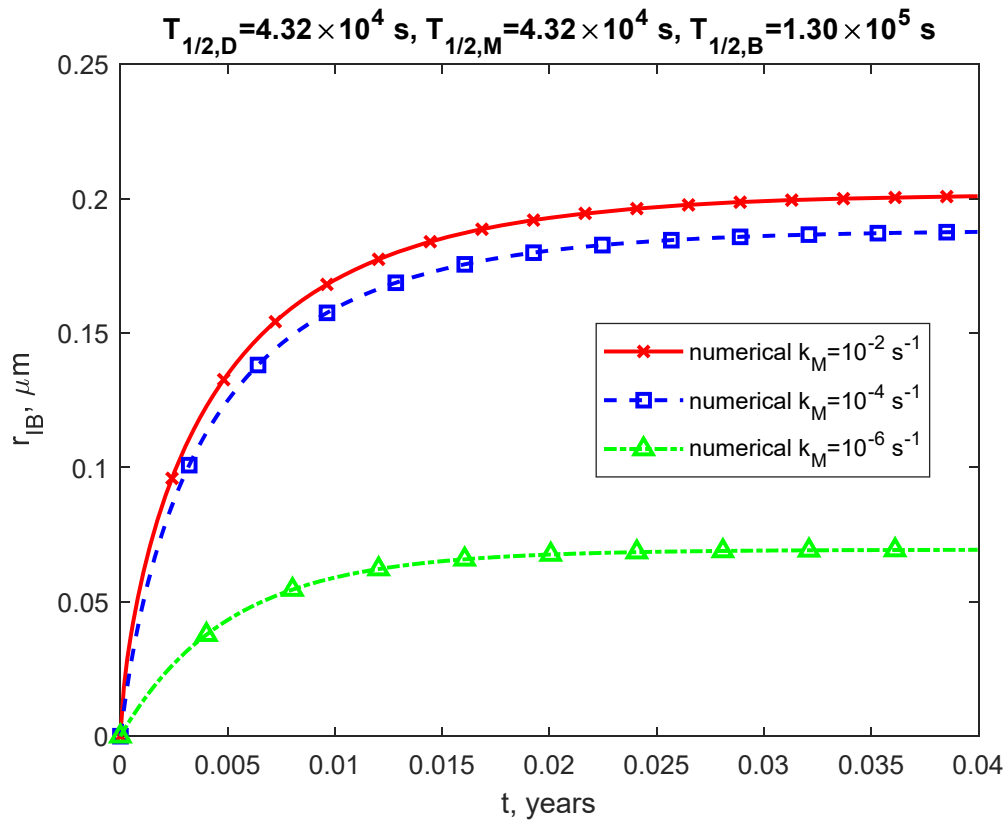
$T_{1/2,D}$=4.32×10^4 s, $T_{1/2,M}$=4.32×10^4 s, $T_{1/2,B}$=1.30×10^5 s
r_{IB}, μm
t, years
numerical k_M=10^-2 s^-1
numerical k_M=10^-4 s^-1
numerical k_M=10^-6 s^-1

Figure 7

(a)

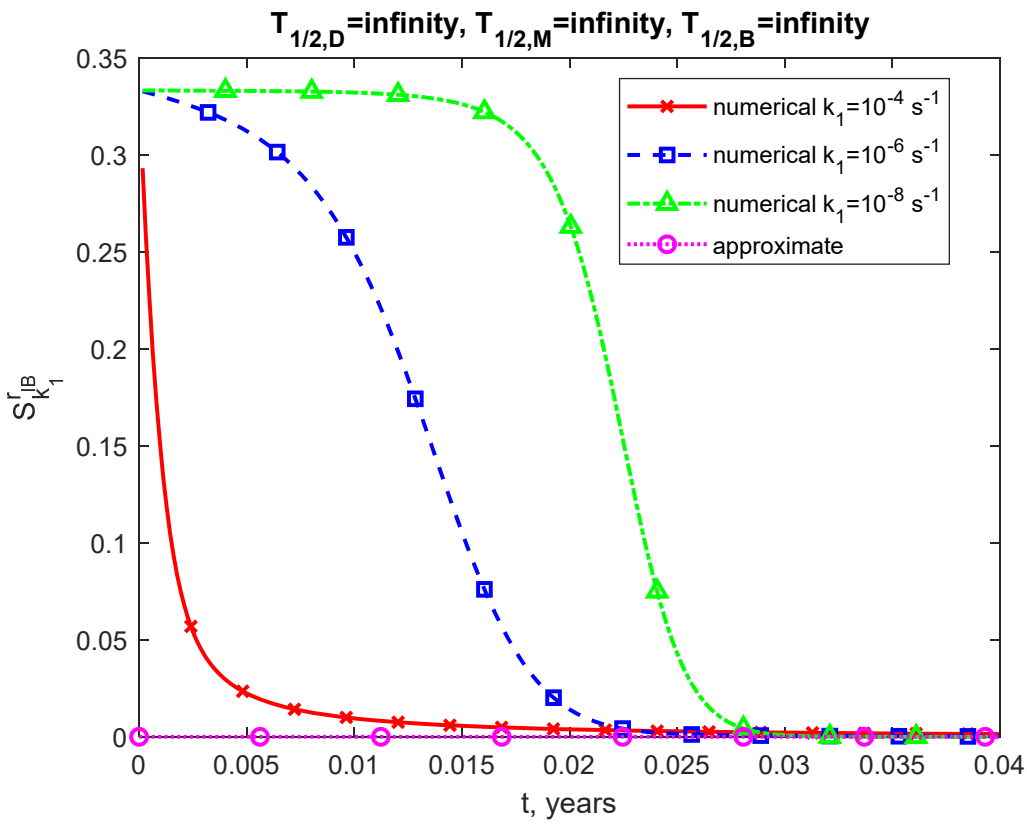

(b)

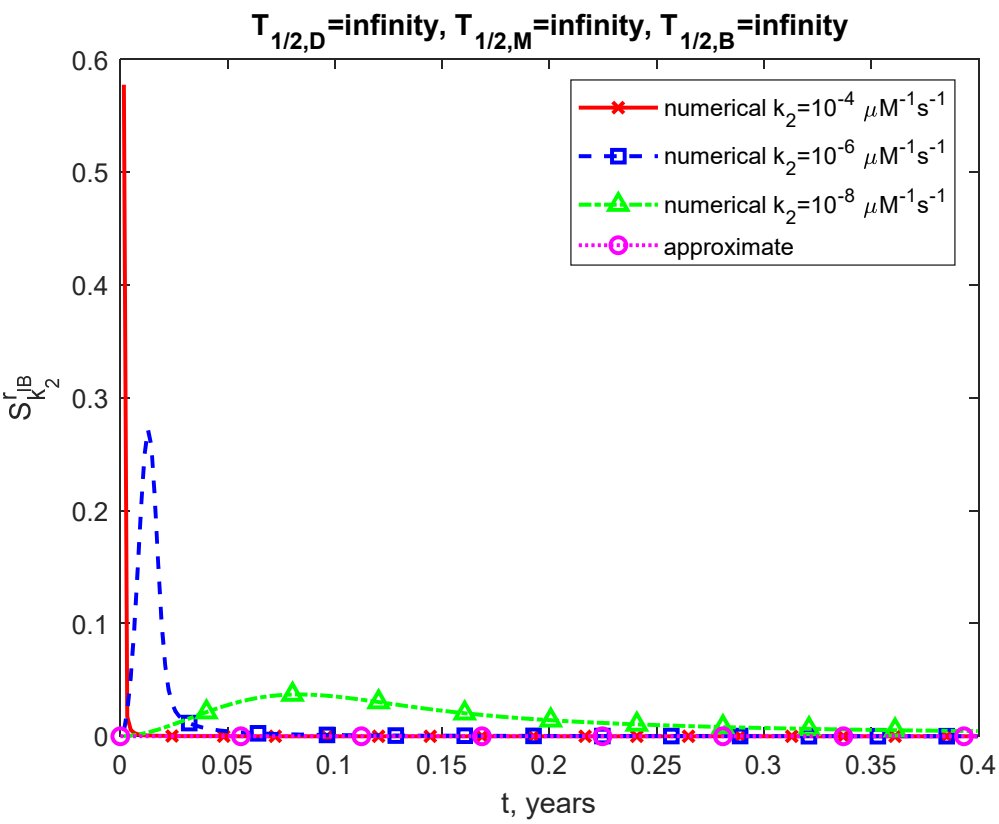

Figure 8a,b

(c)

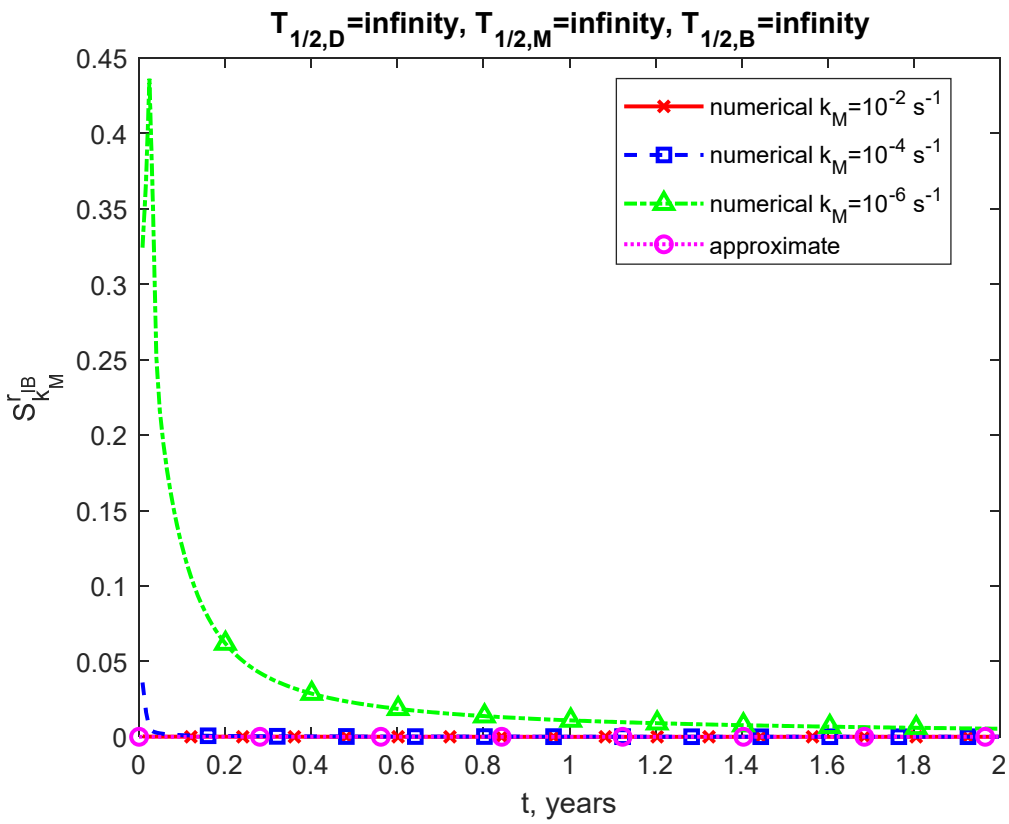
T1/2,D=infinity, T1/2,M=infinity, T1/2,B=infinity
numerical kM=10-2 s-1
numerical kM=10-4 s-1
numerical kM=10-6 s-1
approximate
S r kM IB
t, years
0.45
0.4
0.35
0.3
0.25
0.2
0.15
0.1
0.05
0
0
0.2
0.4
0.6
0.8
1
1.2
1.4
1.6
1.8
2

Figure 8c

Simulating growth of TDP-43 cytosolic inclusion bodies in neurons

Andrey V. Kuznetsov

Department of Mechanical and Aerospace Engineering, North Carolina State University,

Raleigh, NC 27695-7910, USA; e-mail: avkuznet@ncsu.edu

Supplemental Materials

S1. Supplemental tables

Table S1. Data extracted from Table 2 of Morris et al. (2008), presenting best-fit values of rate constants, k_1 and k_2, used for simulating the aggregation of diverse proteins by the F-W model, $A \xrightarrow{k_1} B$, $A + B \xrightarrow{k_2} 2B$ (A denotes monomers and B denotes aggregates). The data reported in Morris et al. (2008) have been converted into SI units to establish representative ranges for k_1 and k_2. This was done because values for k_1 and k_2 specific to TDP-43 are not available in the literature.

Entry (same as in Morris et al. 2008)	System	k_1, s^{-1}	k_2, μM^{-1} s^{-1}	Reference
1	amyloid β	2.2×10^{-9}	6.4×10^{-7}	Bieschke et al. (2005)
2	amyloid β	1×10^{-4}	1.2×10^{-5}	Vestergaard et al. (2005)
3	amyloid β	1.7×10^{-10}	8.3×10^{-2}	Lu et al. (2003)
4	amyloid β, 1 mM peptide	2.8×10^{-8}	1.6×10^{-2}	Dong et al. (2006)
5	amyloid β, [Zn]:[peptide]= 0.2	2.3×10^{-7}	1.8×10^{-2}	Dong et al. (2006)
6	amyloid β, [Zn]:[peptide]= 0.4	4.4×10^{-8}	1.9×10^{-2}	Dong et al. (2006)
7	amyloid β, Aβ 1-16	8.1×10^{-8}	2.1×10^{-5}	Zirah et al. (2006)
8	amyloid β, Aβ 5-16	2.4×10^{-8}	4.1×10^{-5}	Zirah et al. (2006)
9	α-synuclein	1.1×10^{-8}	1.1×10^{-6}	Fink (2006)
10	α-synuclein	2.8×10^{-7}	3.1×10^{-4}	Sode et al. (2005)
11	polyglutamine	7.2×10^{-7}	6.4×10^{-8}	Chen et al. (2002)
12	polyglutamine	2.8×10^{-7}	3.6×10^{-6}	Wetzel (2006)
13	β-microglobulin	1.7×10^{-13}	1.5×10^{-4}	Ban et al. (2006)
14	D67H lysozyme	3.1×10^{-5}	3.9×10^{-5}	Dumoulin et al. (2006)

S2. Supplemental figures

Figs. S1-S9 and Figs. S10-S18 present illustrations of the concentrations of TDP-43 dimers [*D*], monomers [*M*], and aggregates [*B*] under different conditions. Figs. S1-S9 depict a situation with infinite half-lives of TDP-43 dimers, monomers, and aggregates, while Figs. S10-S18 represent a scenario with physiologically relevant half-lives of these proteins. The numerical solution is obtained by solving Eqs. (4)-(6) numerically, with the initial condition (7). The approximate analytical solution depicted in Figs. S1-S9 is computed utilizing Eqs. (8), (12), and (11).

(a)

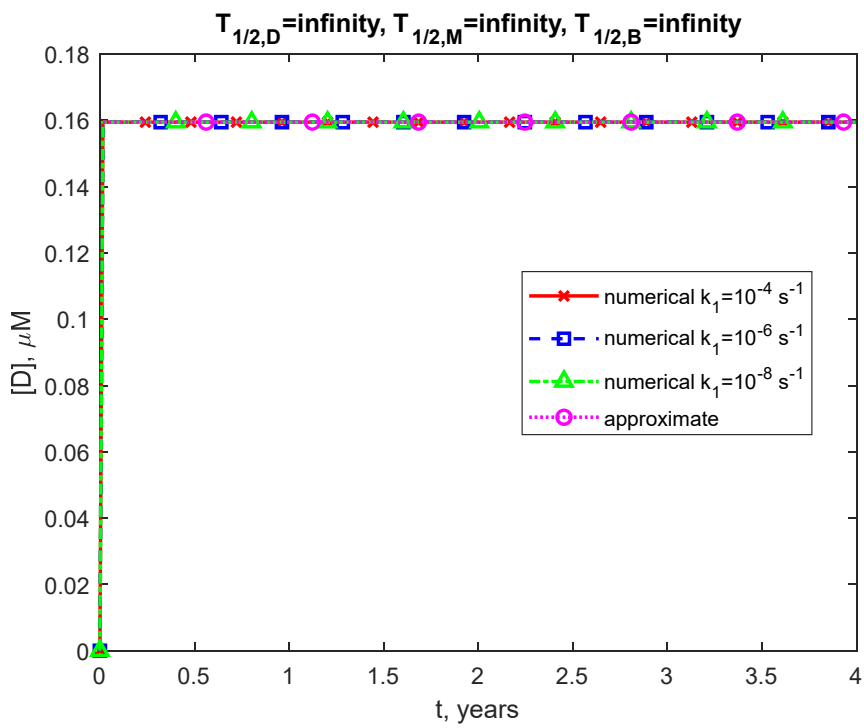

(b)

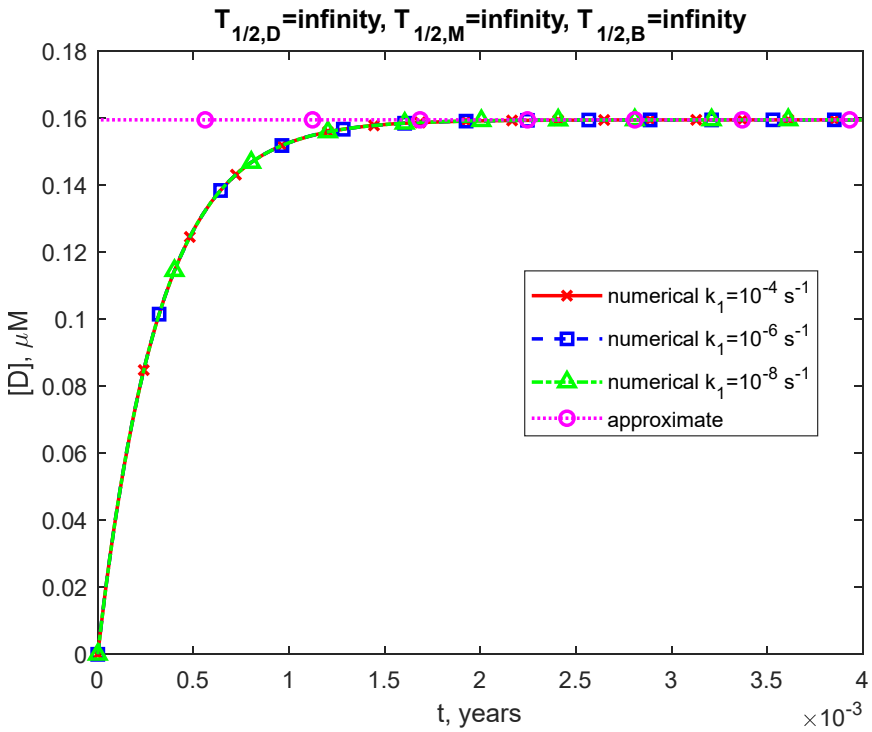

Fig. S1. (a) Molar concentration of TDP-43 dimers, [*D*], over time (in years). (b) Similar to Fig. S1a but focusing on a specific time range of [0 0.004 year] on the *x*-axis. The numerical solution is obtained by solving Eqs. (4)-(6) numerically with the initial condition (7). The approximate solution is determined by employing Eq. (8). The presented scenario assumes dysfunctional protein degradation machinery with $T_{1/2,D} \to \infty$, $T_{1/2,M} \to \infty$, and $T_{1/2,B} \to \infty$. The results are displayed for three values of k_1. $k_2 = 10^{-6}$ μM^{-1} s^{-1} and $k_M = 10^{-4}$ s^{-1}.

(a)

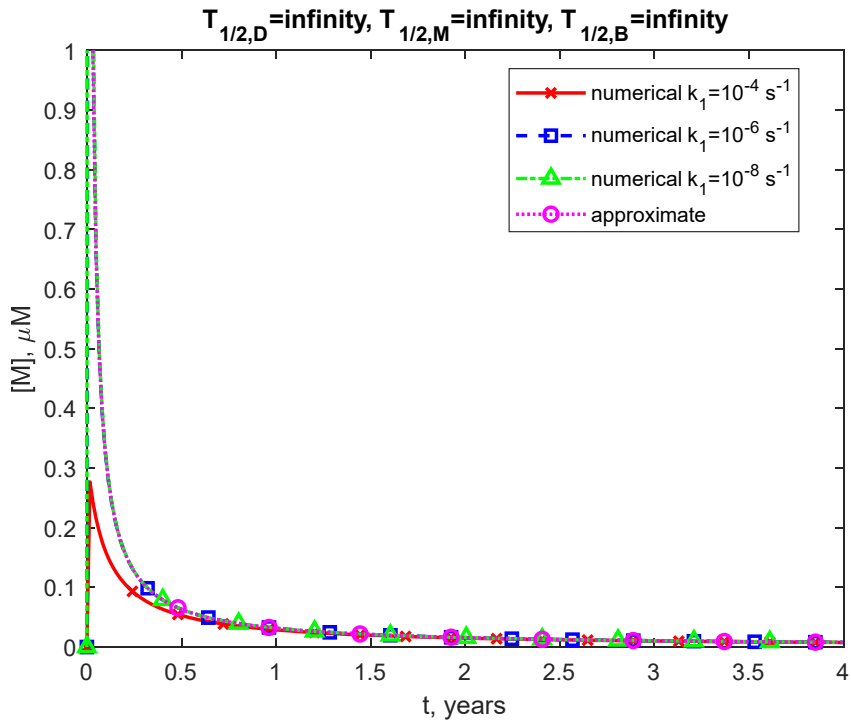

(b)

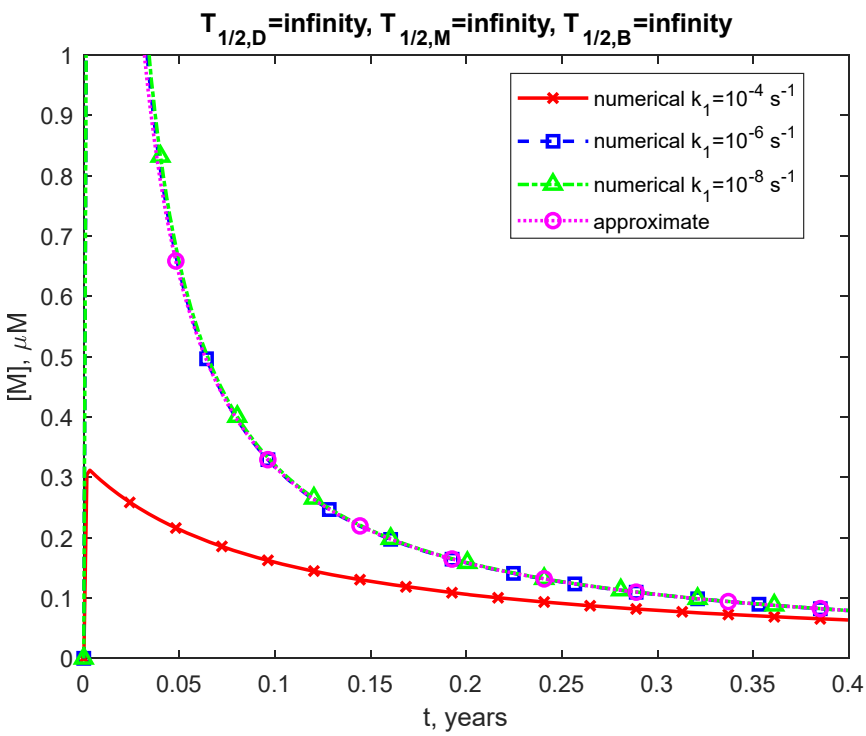

Fig. S2. (a) Molar concentration of TDP-43 monomers, [*M*], over time (in years). (b) Similar to Fig. S2a but focusing on a specific time range of [0 0.4 year] on the *x*-axis. The numerical solution is obtained by

solving Eqs. (4)-(6) numerically with the initial condition (7). The approximate solution is determined by employing Eq. (12). The presented scenario assumes dysfunctional protein degradation machinery with $T_{1/2,D} \to \infty$, $T_{1/2,M} \to \infty$, and $T_{1/2,B} \to \infty$. The results are displayed for three values of k_1. $k_2 = 10^{-6}$ μM^{-1} s^{-1} and $k_M = 10^{-4}$ s^{-1}.

(a)

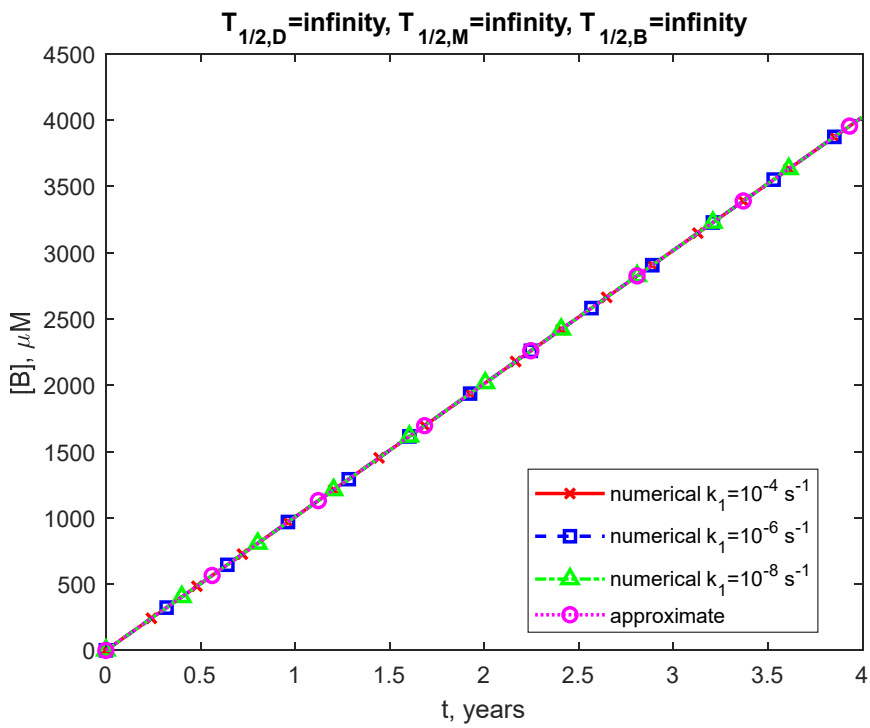

(b)

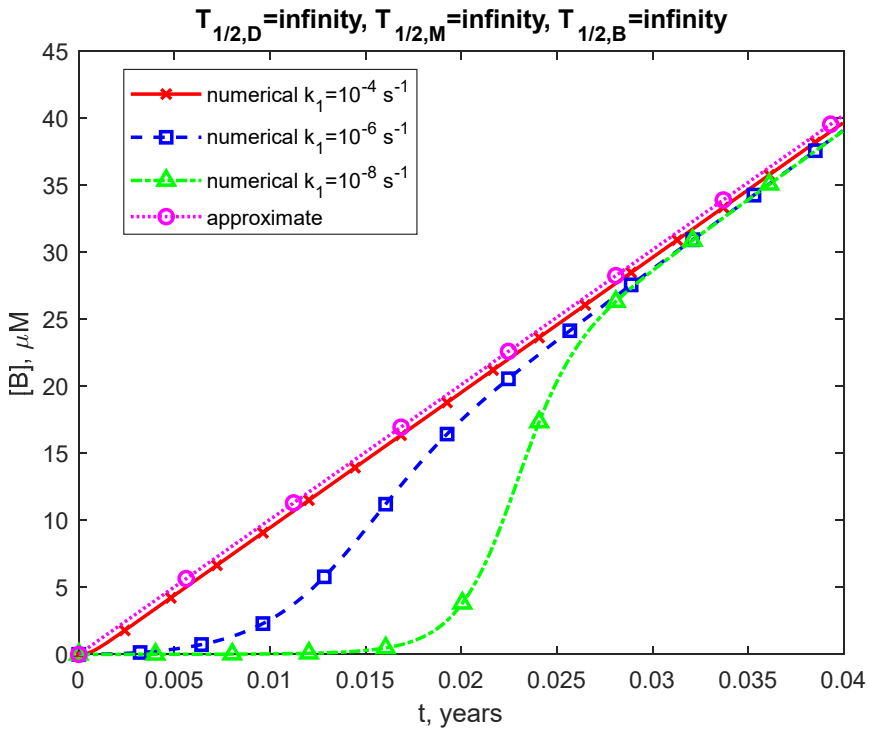

Fig. S3. (a) Molar concentration of TDP-43 aggregates, [*B*], over time (in years). (b) Similar to Fig. S3a but focusing on a specific time range of [0 0.04 year] on the *x*-axis. The numerical solution is obtained by solving Eqs. (4)-(6) numerically with the initial condition (7). The approximate solution is determined by employing Eq. (11). The presented scenario assumes dysfunctional protein degradation machinery with $T_{1/2,D} \to \infty$, $T_{1/2,M} \to \infty$, and $T_{1/2,B} \to \infty$. The results are displayed for three values of k_1. $k_2 = 10^{-6}$ μM^{-1} s^{-1} and $k_M = 10^{-4}$ s^{-1}.

(a)

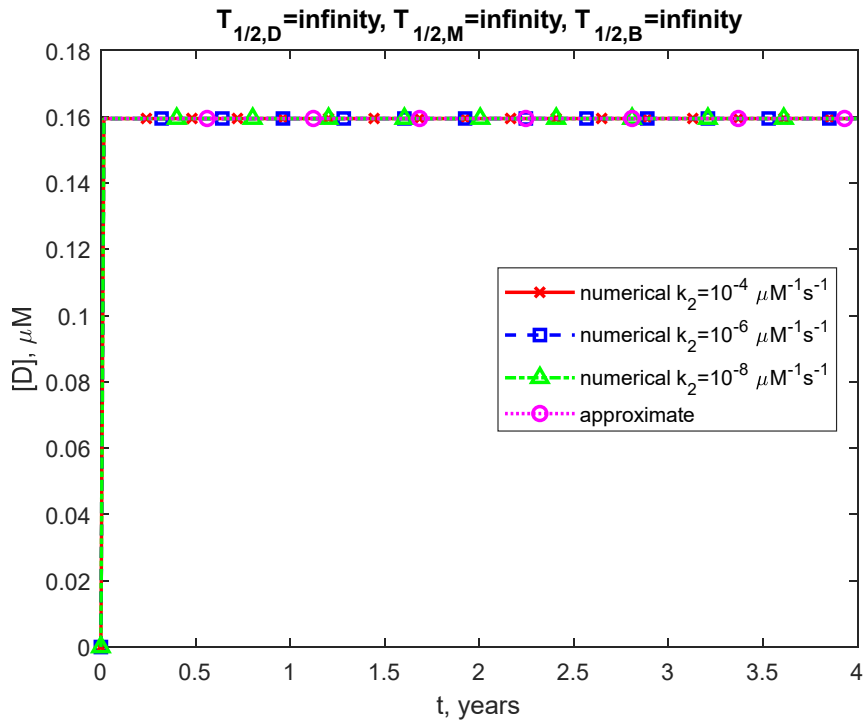

(b)

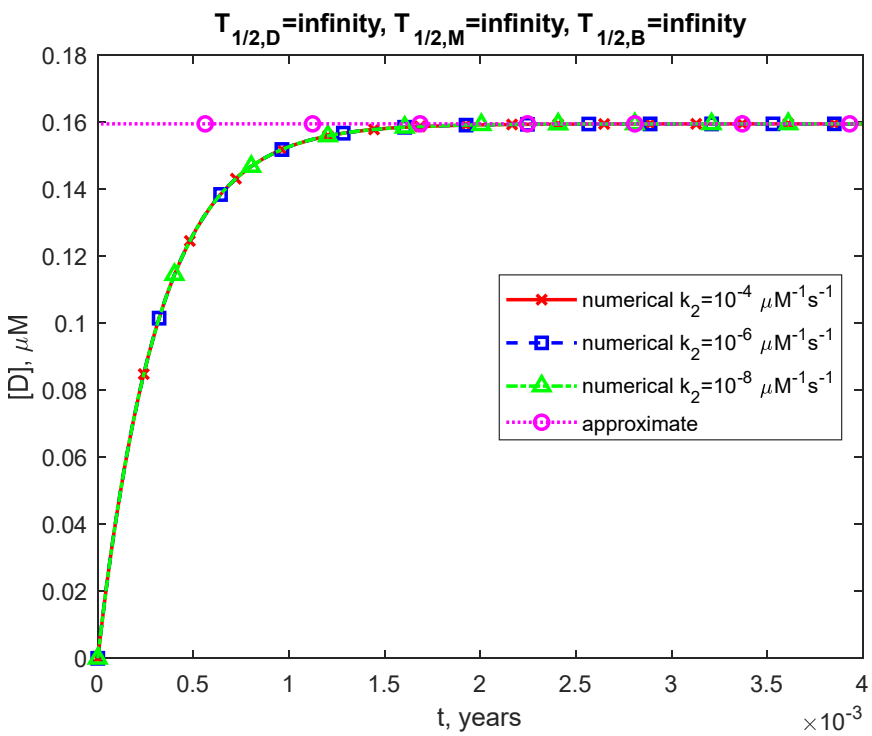

Fig. S4. (a) Molar concentration of TDP-43 dimers, [*D*], over time (in years). (b) Similar to Fig. S4a but focusing on a specific time range of [0 0.004 year] on the *x*-axis. The numerical solution is obtained by

solving Eqs. (4)-(6) numerically with the initial condition (7). The approximate solution is determined by employing Eq. (8). The presented scenario assumes dysfunctional protein degradation machinery with $T_{1/2,D} \to \infty$, $T_{1/2,M} \to \infty$, and $T_{1/2,B} \to \infty$. The results are displayed for three values of k_2. $k_1 = 10^{-6}$ s^{-1} and $k_M = 10^{-4}$ s^{-1}.

(a)

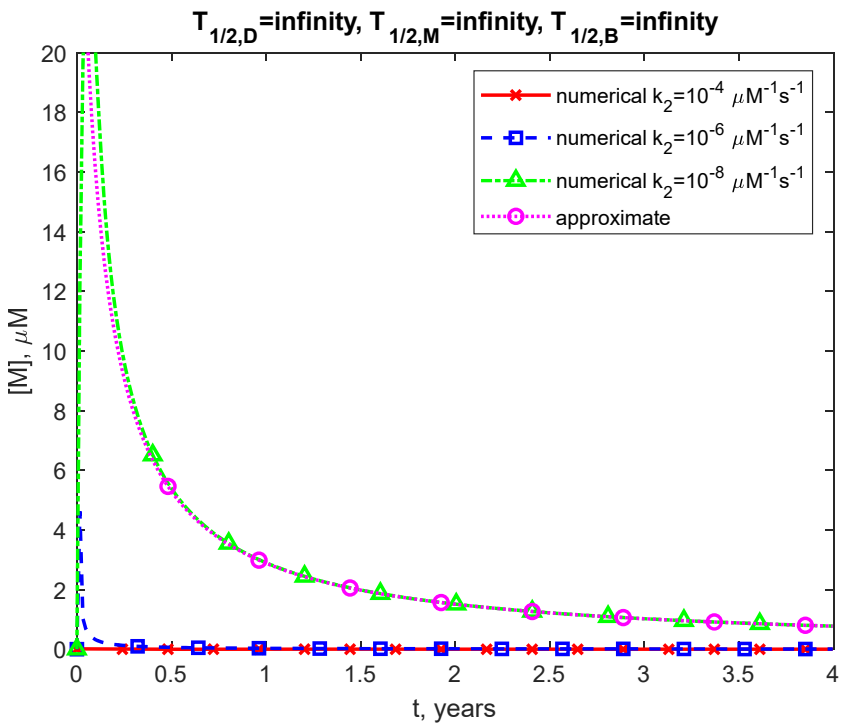

(b)

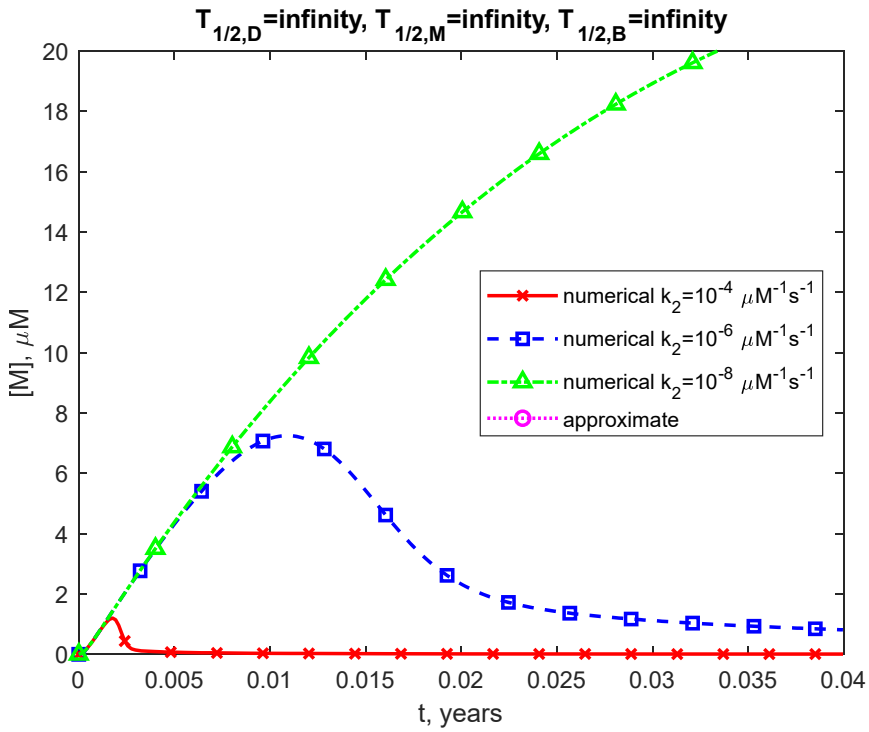

Fig. S5. (a) Molar concentration of TDP-43 monomers, [*M*], over time (in years). (b) Similar to Fig. S5a but focusing on a specific time range of [0 0.04 year] on the *x*-axis. The numerical solution is obtained by solving Eqs. (4)-(6) numerically with the initial condition (7). The approximate solution is determined by employing Eq. (12). The presented scenario assumes dysfunctional protein degradation machinery with $T_{1/2,D} \to \infty$, $T_{1/2,M} \to \infty$, and $T_{1/2,B} \to \infty$. The results are displayed for three values of k_2. $k_1 = 10^{-6}$ s^{-1} and $k_M = 10^{-4}$ s^{-1}.

(a)

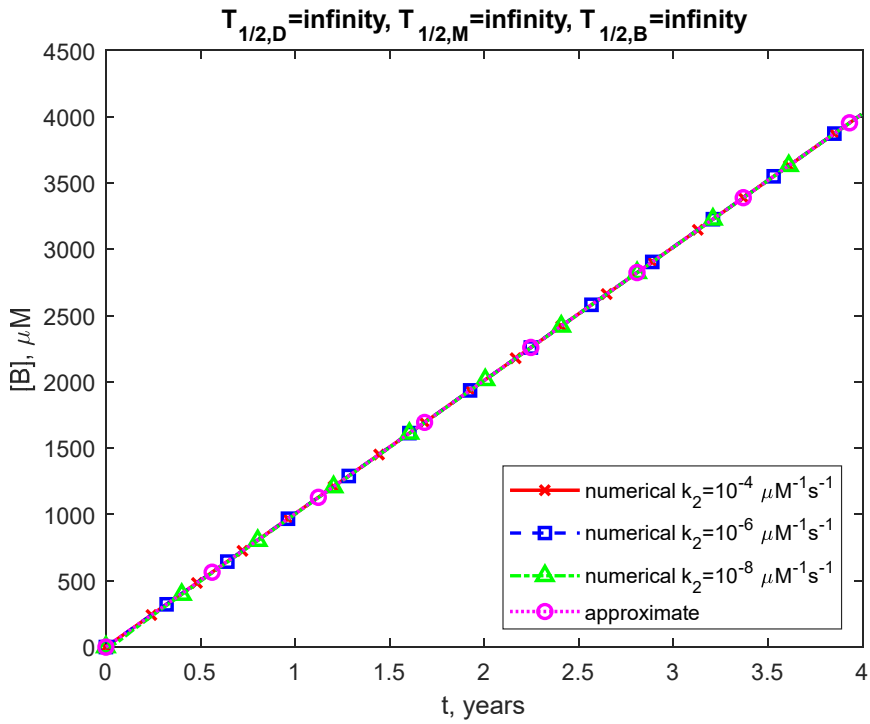

(b)

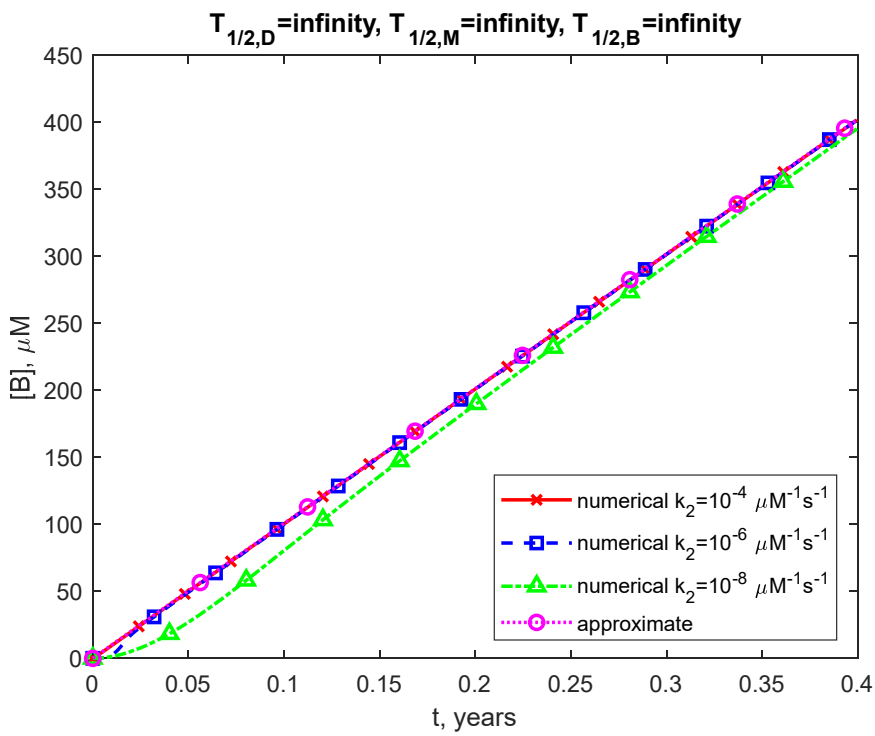

Fig. S6. (a) Molar concentration of TDP-43 aggregates, [*B*], over time (in years). (b) Similar to Fig. S6a but focusing on a specific time range of [0 0.4 year] on the *x*-axis. The numerical solution is obtained by

solving Eqs. (4)-(6) numerically with the initial condition (7). The approximate solution is determined by employing Eq. (11). The presented scenario assumes dysfunctional protein degradation machinery with $T_{1/2,D} \to \infty$, $T_{1/2,M} \to \infty$, and $T_{1/2,B} \to \infty$. The results are displayed for three values of k_2. $k_1 = 10^{-6}$ s^{-1} and $k_M = 10^{-4}$ s^{-1}.

(a)

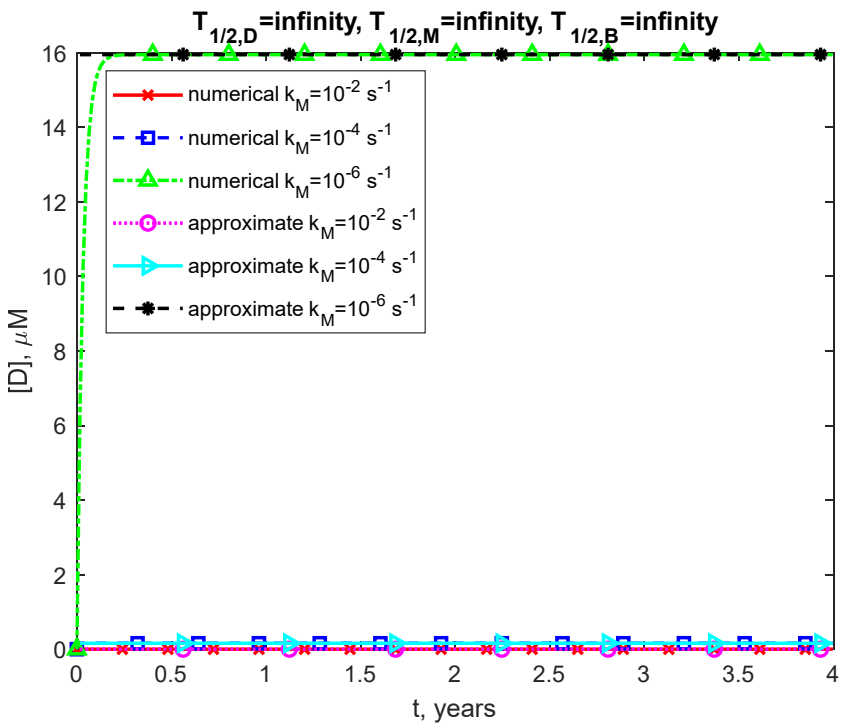

(b)

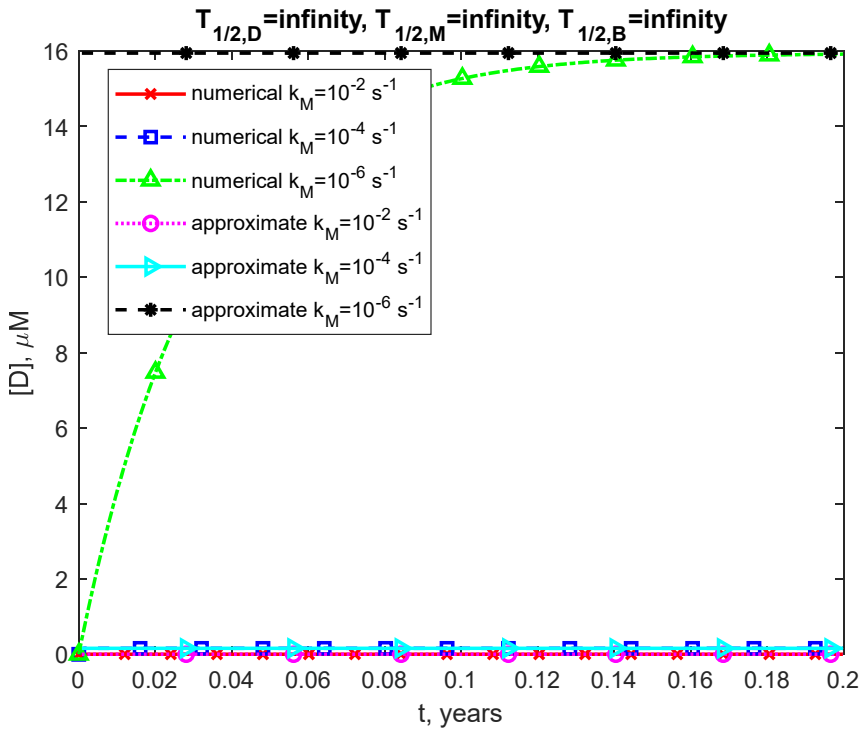

Fig. S7. (a) Molar concentration of TDP-43 dimers, [*D*], over time (in years). (b) Similar to Fig. S7a but focusing on a specific time range of [0 0.2 year] on the *x*-axis. The numerical solution is obtained by solving Eqs. (4)-(6) numerically with the initial condition (7). The approximate solution is determined by employing Eq. (8). The presented scenario assumes dysfunctional protein degradation machinery with $T_{1/2,D} \to \infty$, $T_{1/2,M} \to \infty$, and $T_{1/2,B} \to \infty$. The results are displayed for three values of k_M. $k_1 = 10^{-6}$ s^{-1} and $k_2 = 10^{-6}$ μM^{-1} s^{-1}.

(a)

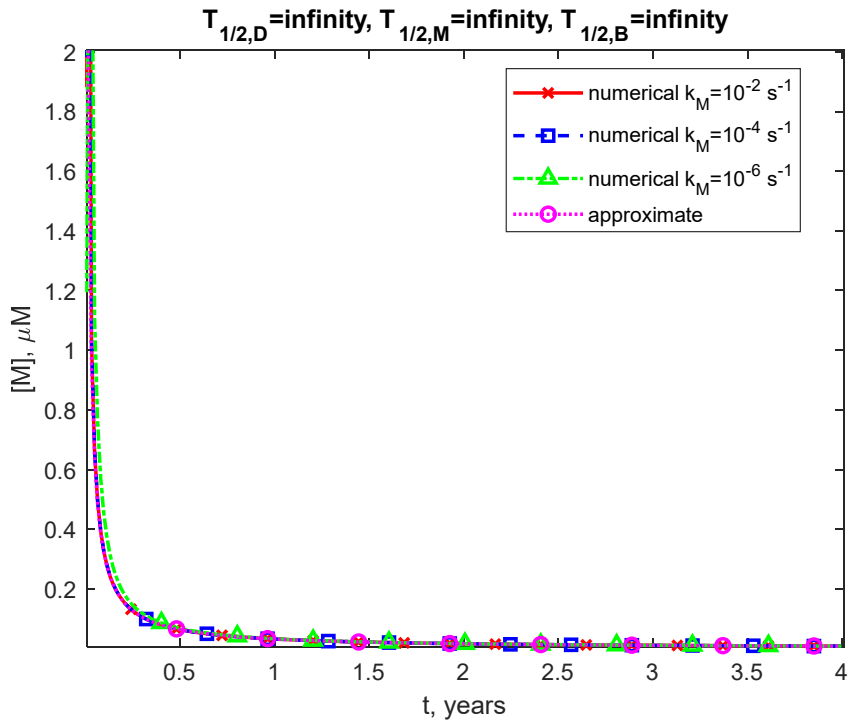

(b)

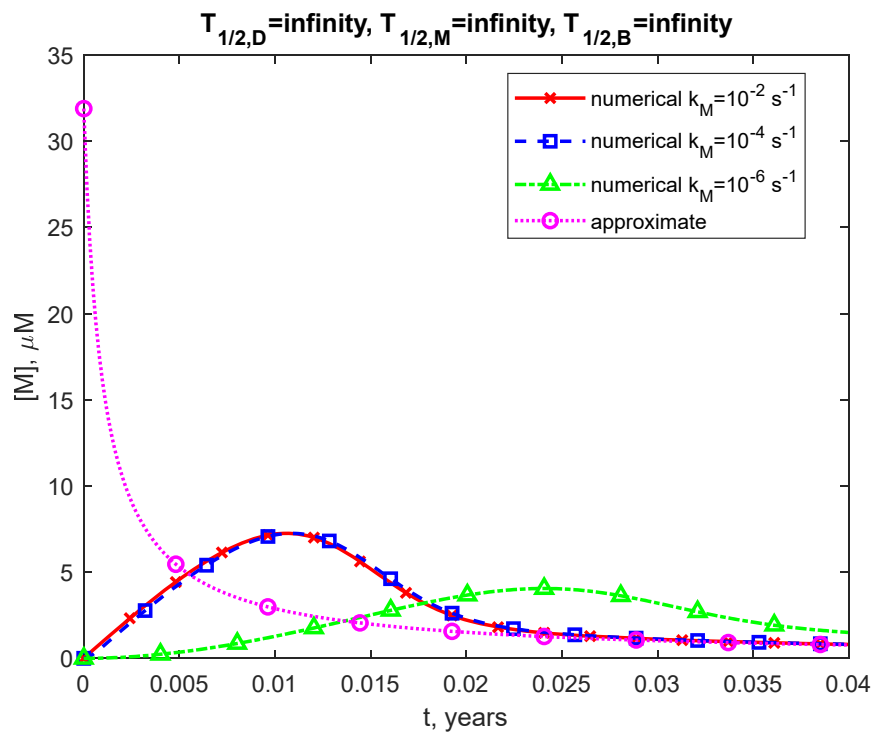

Fig. S8. (a) Molar concentration of TDP-43 monomers, [*M*], over time (in years). (b) Similar to Fig. S8a but focusing on a specific time range of [0 0.04 year] on the *x*-axis. The numerical solution is obtained by

solving Eqs. (4)-(6) numerically with the initial condition (7). The approximate solution is determined by employing Eq. (12). The presented scenario assumes dysfunctional protein degradation machinery with $T_{1/2,D} \to \infty$, $T_{1/2,M} \to \infty$, and $T_{1/2,B} \to \infty$. The results are displayed for three values of k_M. $k_1 = 10^{-6}$ s^{-1} and $k_2 = 10^{-6}$ μM^{-1} s^{-1}.

(a)

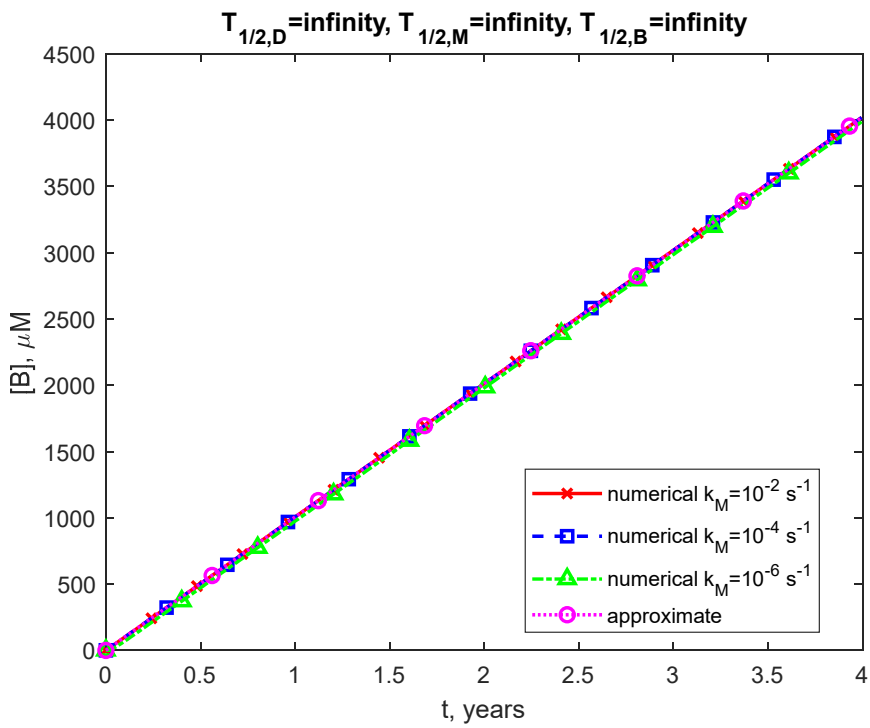

(b)

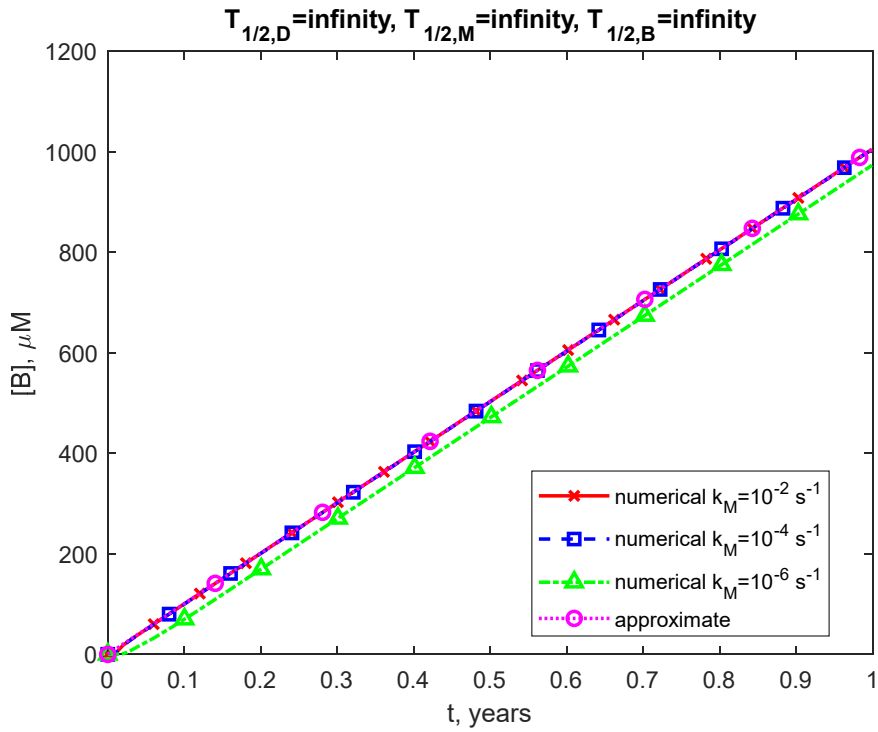

Fig. S9. (a) Molar concentration of TDP-43 aggregates, [*B*], over time (in years). (b) Similar to Fig. S9a but focusing on a specific time range of [0 1 year] on the *x*-axis. The numerical solution is obtained by solving Eqs. (4)-(6) numerically with the initial condition (7). The approximate solution is determined by employing Eq. (11). The presented scenario assumes dysfunctional protein degradation machinery with $T_{1/2,D} \to \infty$, $T_{1/2,M} \to \infty$, and $T_{1/2,B} \to \infty$. The results are displayed for three values of k_M. $k_1 = 10^{-6}$ s^{-1} and $k_2 = 10^{-6}$ μM^{-1} s^{-1}.

(a)

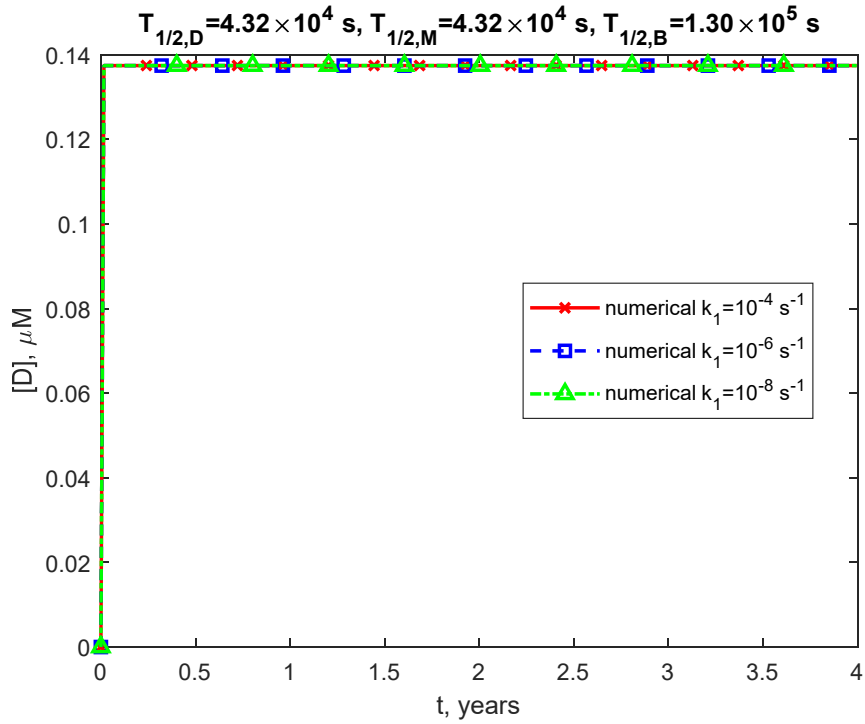

(b)

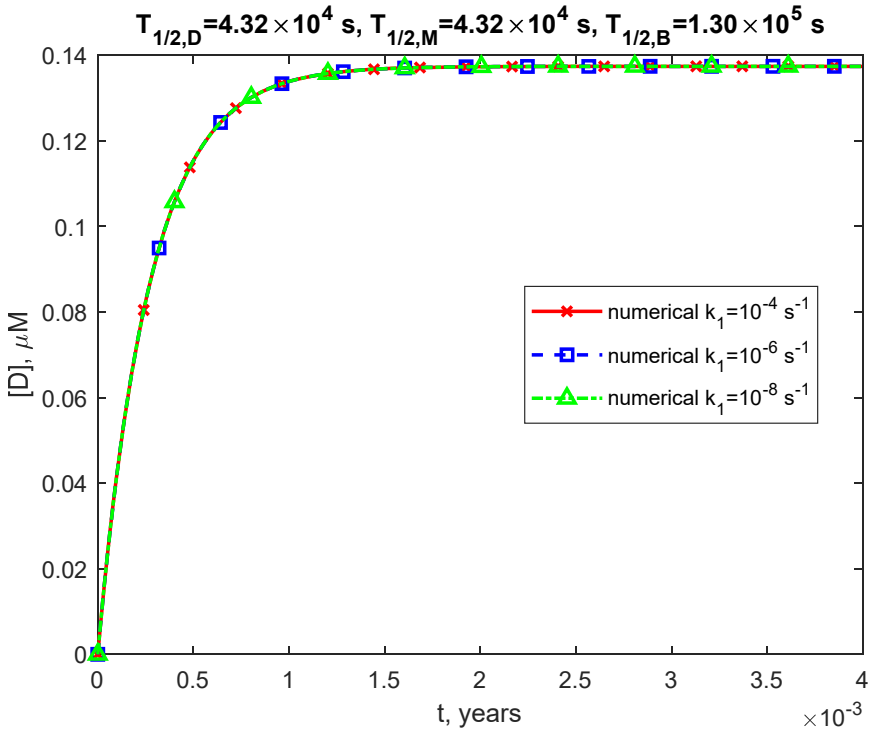

Fig. S10. (a) Molar concentration of TDP-43 dimers, [*D*], over time (in years). (b) Similar to Fig. S10a but focusing on a specific time range of [0 0.004 year] on the *x*-axis. The numerical solution is obtained

by solving Eqs. (4)-(6) numerically with the initial condition (7). The presented scenario assumes physiologically relevant values for the half-lives of TDP-43 dimers, monomers, and aggregates. $T_{1/2,D} = 4.32\times10^4$ s, $T_{1/2,M} = 4.32\times10^4$ s, and $T_{1/2,B} = 1.30\times10^5$ s. The approximate solution is not displayed as it applies exclusively to the scenario involving infinite half-lives of TDP-43 dimers, monomers, and aggregates. The results are displayed for three values of k_1. $k_2 = 10^{-6}$ μM^{-1} s^{-1} and $k_M = 10^{-4}$ s^{-1}.

(a)

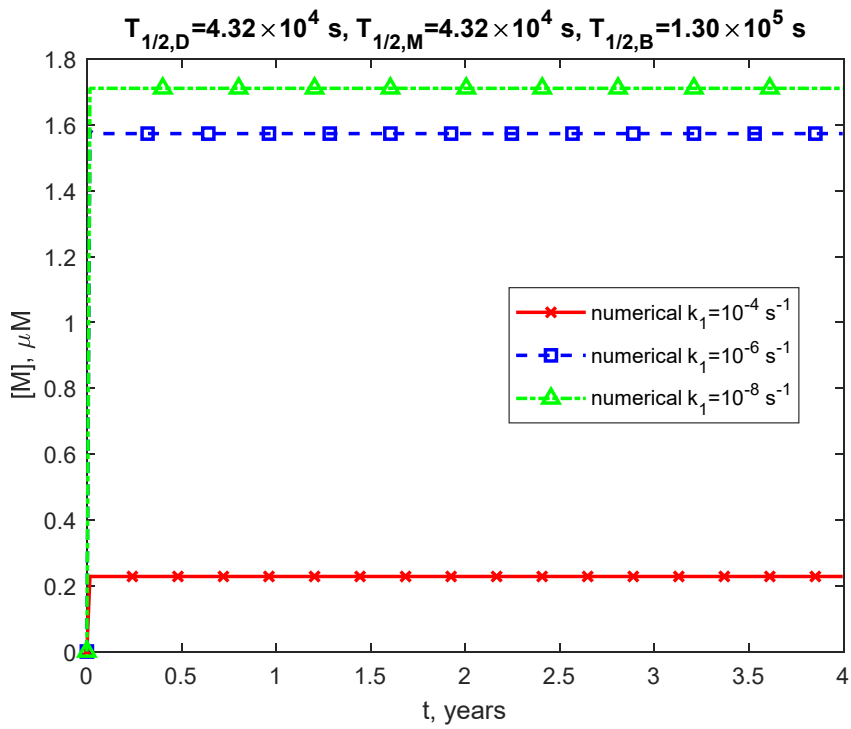

(b)

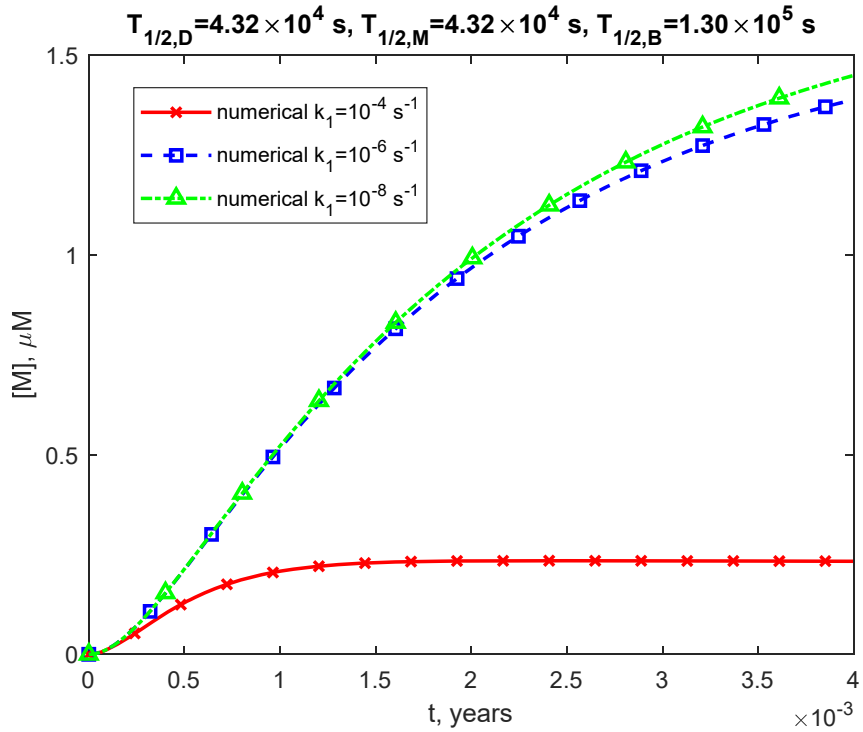

Fig. S11. (a) Molar concentration of TDP-43 monomers, [*M*], over time (in years). (b) Similar to Fig. S11a but focusing on a specific time range of [0 0.004 year] on the *x*-axis. The numerical solution is obtained by solving Eqs. (4)-(6) numerically with the initial condition (7). The presented scenario assumes physiologically relevant values for the half-lives of TDP-43 dimers, monomers, and aggregates. $T_{1/2,D} = 4.32\times10^4$ s, $T_{1/2,M} = 4.32\times10^4$ s, and $T_{1/2,B} = 1.30\times10^5$ s. The approximate solution is not displayed as it applies exclusively to the scenario involving infinite half-lives of TDP-43 dimers, monomers, and aggregates. The results are displayed for three values of k_1. $k_2 = 10^{-6}$ μM^{-1} s^{-1} and $k_M = 10^{-4}$ s^{-1}.

(a)

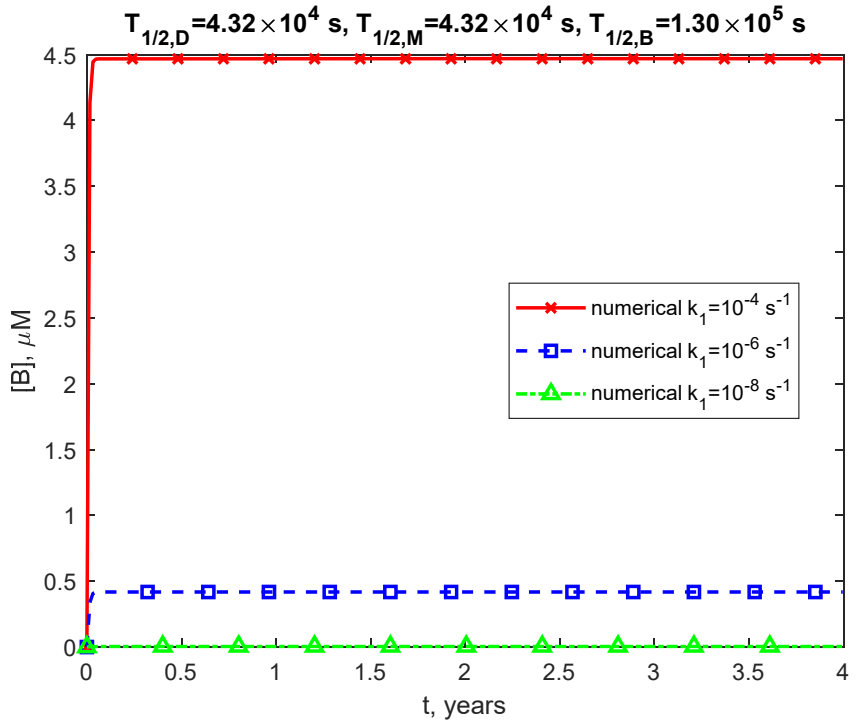

(b)

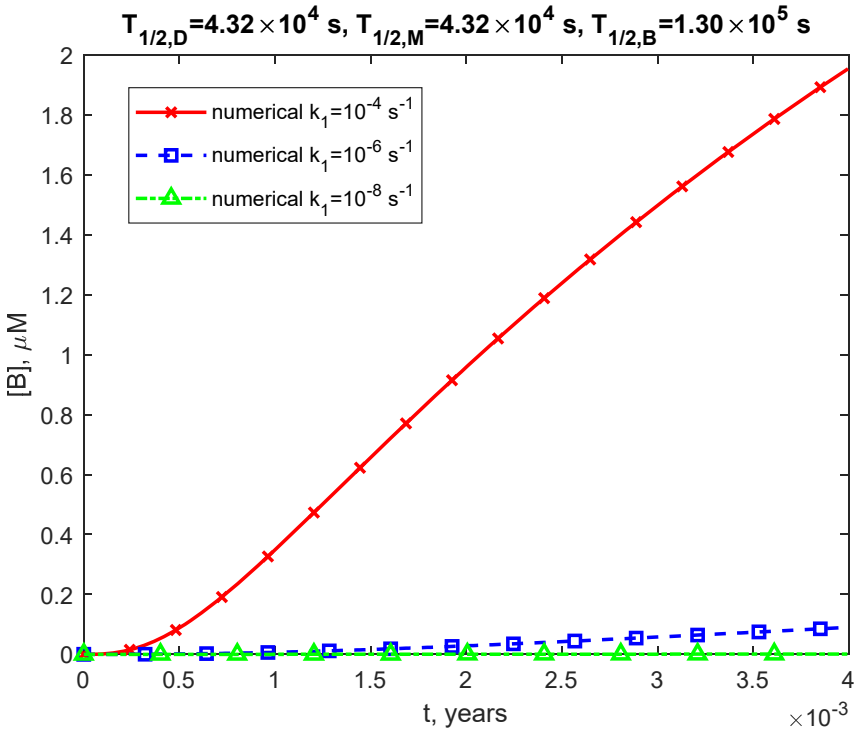

Fig. S12. (a) Molar concentration of TDP-43 aggregates, [*B*], over time (in years). (b) Similar to Fig. S12a but focusing on a specific time range of [0 0.004 year] on the *x*-axis. The numerical solution is

obtained by solving Eqs. (4)-(6) numerically with the initial condition (7). The presented scenario assumes physiologically relevant values for the half-lives of TDP-43 dimers, monomers, and aggregates. $T_{1/2,D} = 4.32\times10^4$ s, $T_{1/2,M} = 4.32\times10^4$ s, and $T_{1/2,B} = 1.30\times10^5$ s. The approximate solution is not displayed as it applies exclusively to the scenario involving infinite half-lives of TDP-43 dimers, monomers, and aggregates. The results are displayed for three values of k_1. $k_2 = 10^{-6}$ μM^{-1} s^{-1} and $k_M = 10^{-4}$ s^{-1}.

(a)

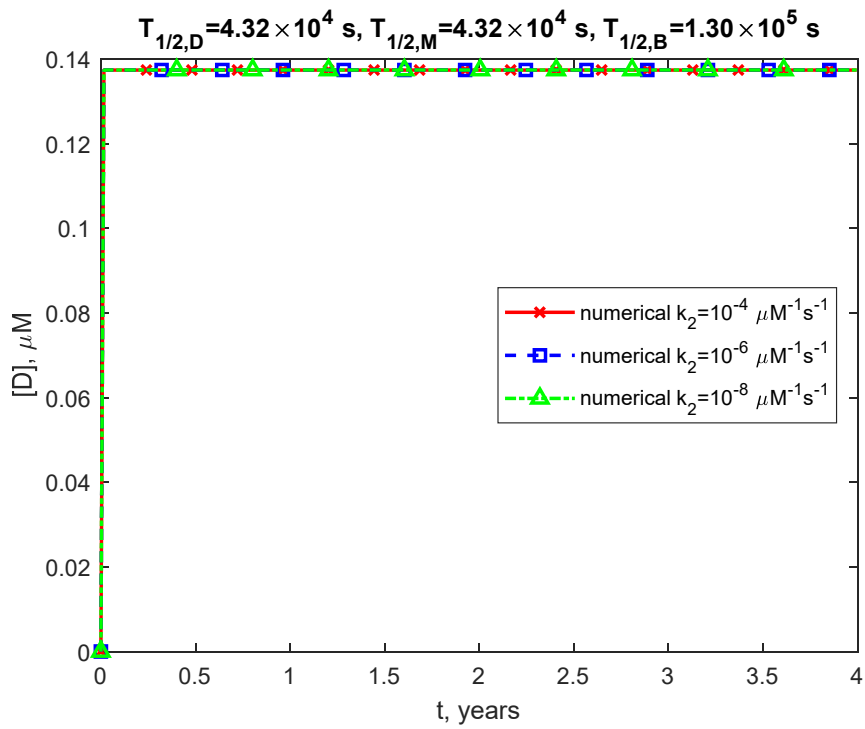

(b)

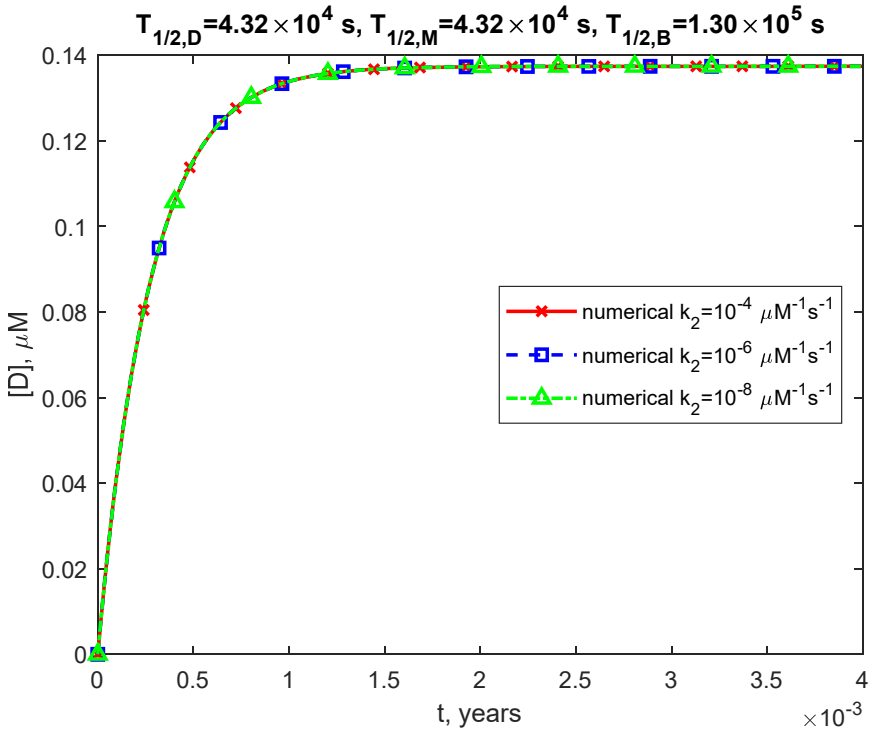

Fig. S13. (a) Molar concentration of TDP-43 dimers, [*D*], over time (in years). (b) Similar to Fig. S13a but focusing on a specific time range of [0 0.004 year] on the *x*-axis. The numerical solution is obtained by solving Eqs. (4)-(6) numerically with the initial condition (7). The presented scenario assumes physiologically relevant values for the half-lives of TDP-43 dimers, monomers, and aggregates. $T_{1/2,D} = 4.32\times10^4$ s, $T_{1/2,M} = 4.32\times10^4$ s, and $T_{1/2,B} = 1.30\times10^5$ s. The approximate solution is not displayed as it applies exclusively to the scenario involving infinite half-lives of TDP-43 dimers, monomers, and aggregates. The results are displayed for three values of k_2. $k_1 = 10^{-6}$ s^{-1} and $k_M = 10^{-4}$ s^{-1}.

(a)

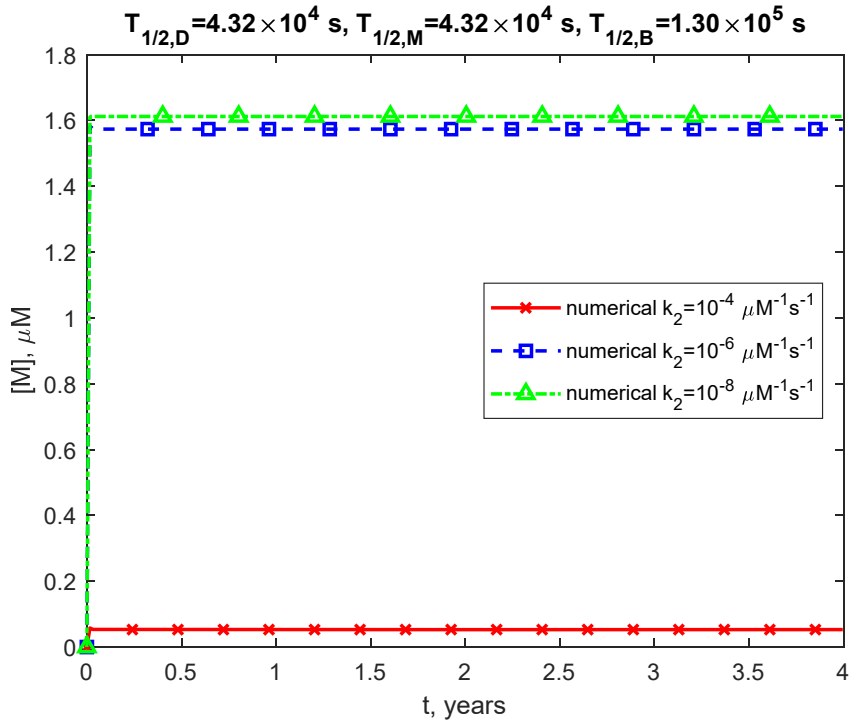

(b)

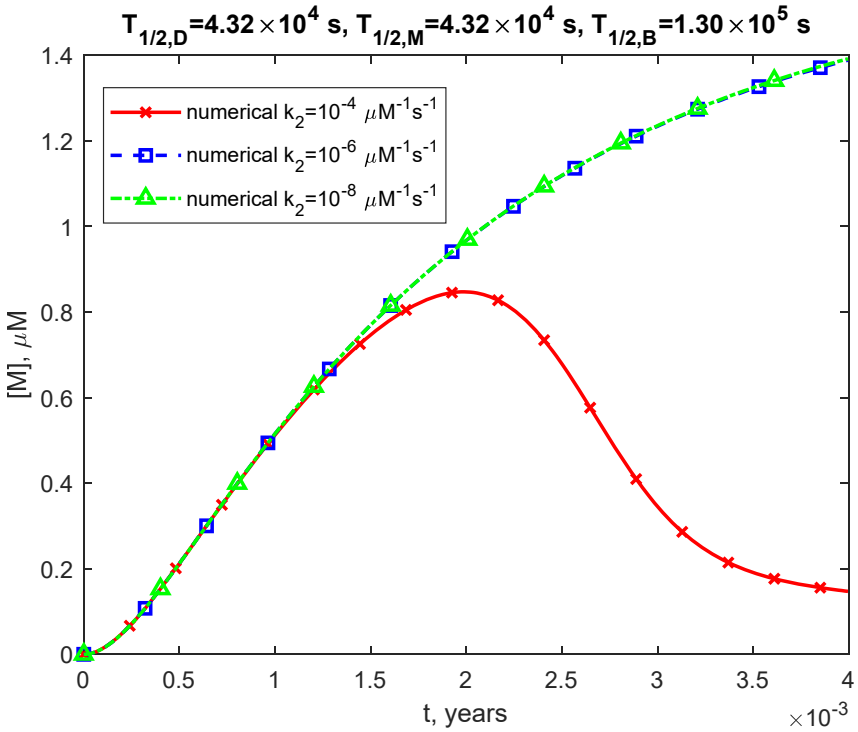

Fig. S14. (a) Molar concentration of TDP-43 monomers, [*M*], over time (in years). (b) Similar to Fig. S14a but focusing on a specific time range of [0 0.004 year] on the *x*-axis. The numerical solution is

obtained by solving Eqs. (4)-(6) numerically with the initial condition (7). The presented scenario assumes physiologically relevant values for the half-lives of TDP-43 dimers, monomers, and aggregates. $T_{1/2,D} = 4.32\times10^4$ s, $T_{1/2,M} = 4.32\times10^4$ s, and $T_{1/2,B} = 1.30\times10^5$ s. The approximate solution is not displayed as it applies exclusively to the scenario involving infinite half-lives of TDP-43 dimers, monomers, and aggregates. The results are displayed for three values of k_2. $k_1 = 10^{-6}$ s^{-1} and $k_M = 10^{-4}$ s^{-1}.

(a)

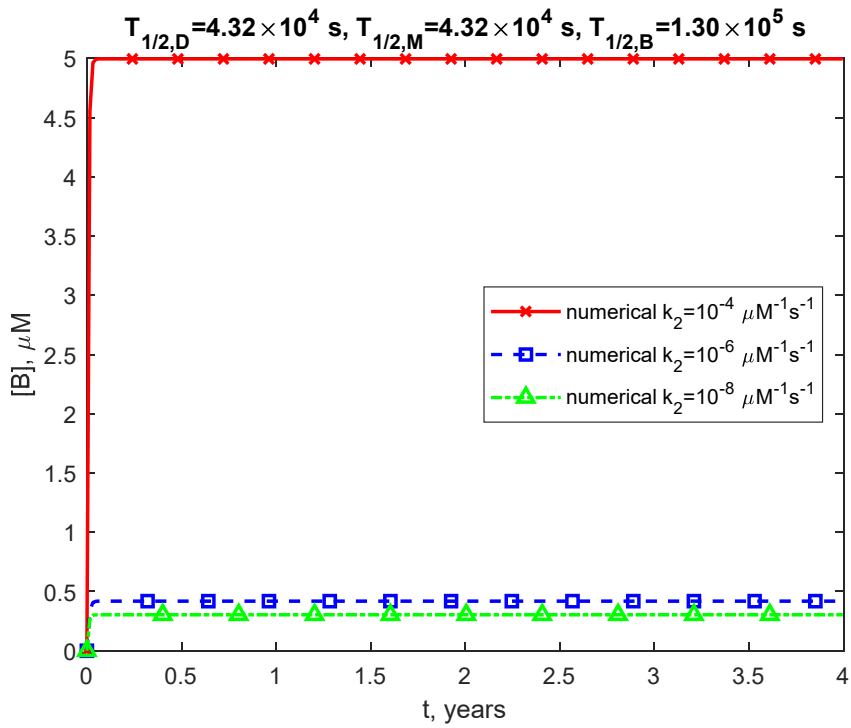

(b)

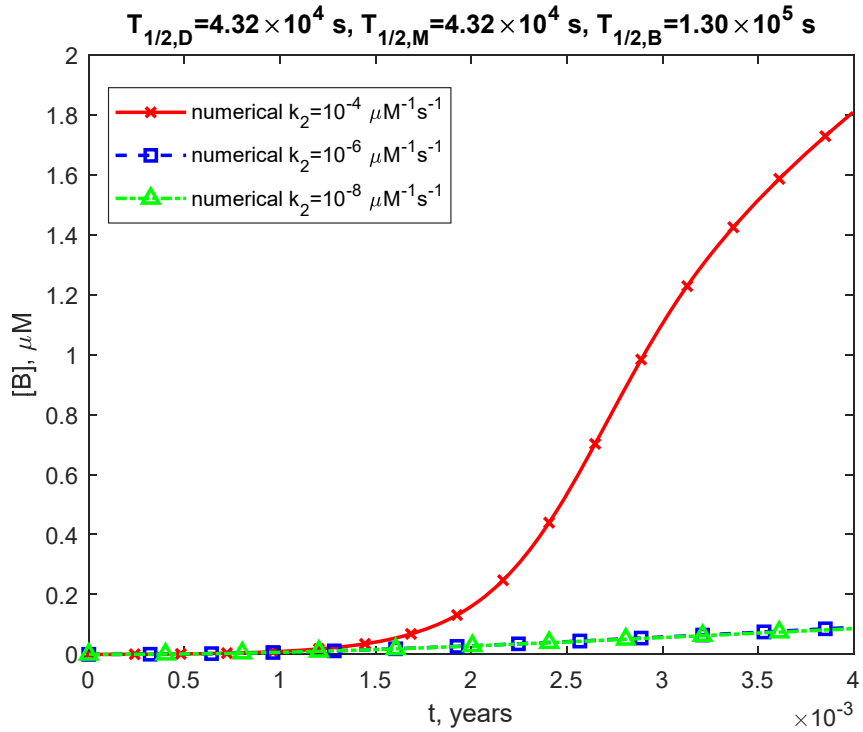

Fig. S15. (a) Molar concentration of TDP-43 aggregates, [*B*], over time (in years). (b) Similar to Fig. S15a but focusing on a specific time range of [0 0.004 year] on the *x*-axis. The numerical solution is obtained by solving Eqs. (4)-(6) numerically with the initial condition (7). The presented scenario assumes physiologically relevant values for the half-lives of TDP-43 dimers, monomers, and aggregates. $T_{1/2,D} = 4.32\times10^4$ s, $T_{1/2,M} = 4.32\times10^4$ s, and $T_{1/2,B} = 1.30\times10^5$ s. The approximate solution is not displayed as it applies exclusively to the scenario involving infinite half-lives of TDP-43 dimers, monomers, and aggregates. The results are displayed for three values of k_2. $k_1 = 10^{-6}$ s^{-1} and $k_M = 10^{-4}$ s^{-1}.

(a)

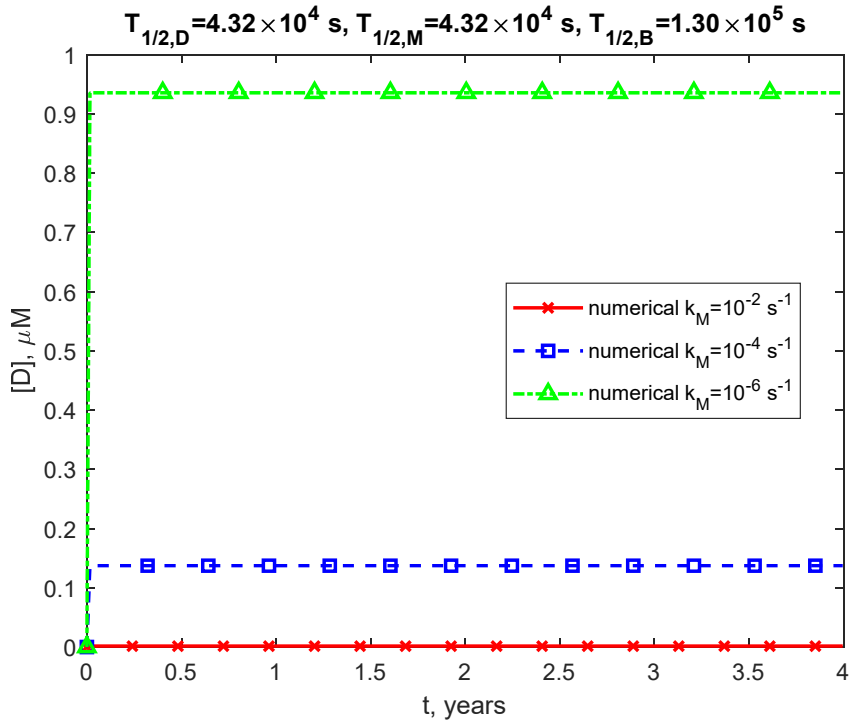

(b)

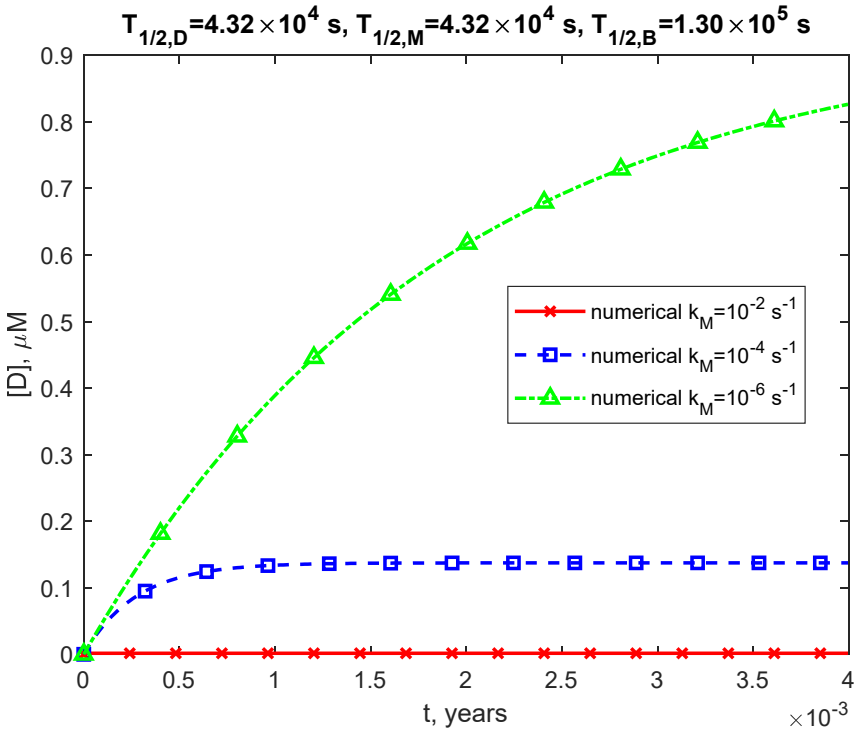

Fig. S16. (a) Molar concentration of TDP-43 dimers, [*D*], over time (in years). (b) Similar to Fig. S16a but focusing on a specific time range of [0 0.004 year] on the *x*-axis. The numerical solution is obtained

by solving Eqs. (4)-(6) numerically with the initial condition (7). The presented scenario assumes physiologically relevant values for the half-lives of TDP-43 dimers, monomers, and aggregates. $T_{1/2,D} = 4.32\times10^4$ s, $T_{1/2,M} = 4.32\times10^4$ s, and $T_{1/2,B} = 1.30\times10^5$ s. The approximate solution is not displayed as it applies exclusively to the scenario involving infinite half-lives of TDP-43 dimers, monomers, and aggregates. The results are displayed for three values of k_M. $k_1 = 10^{-6}$ s^{-1} and $k_2 = 10^{-6}$ μM^{-1} s^{-1}.

(a)

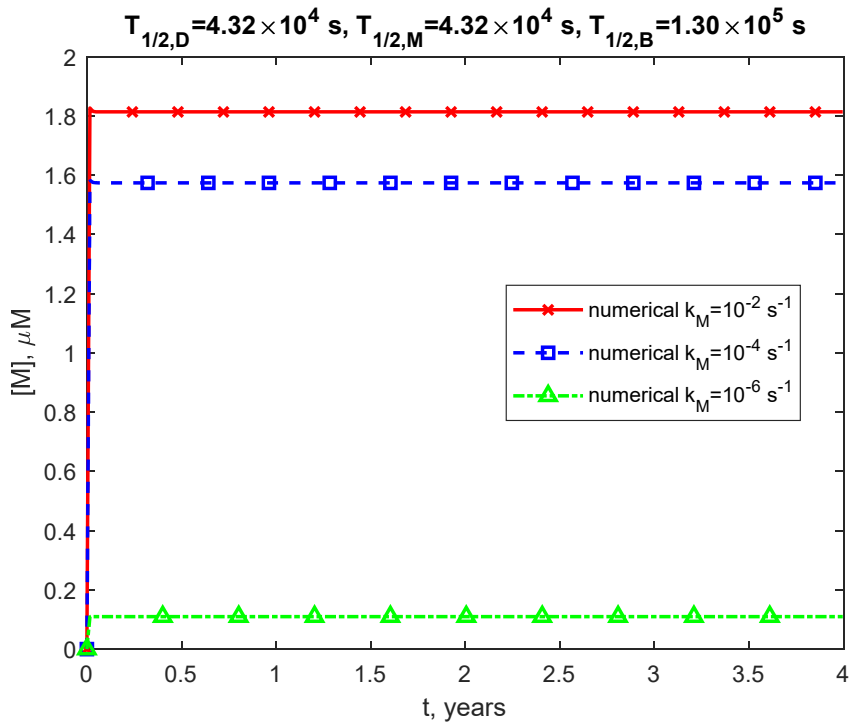

(b)

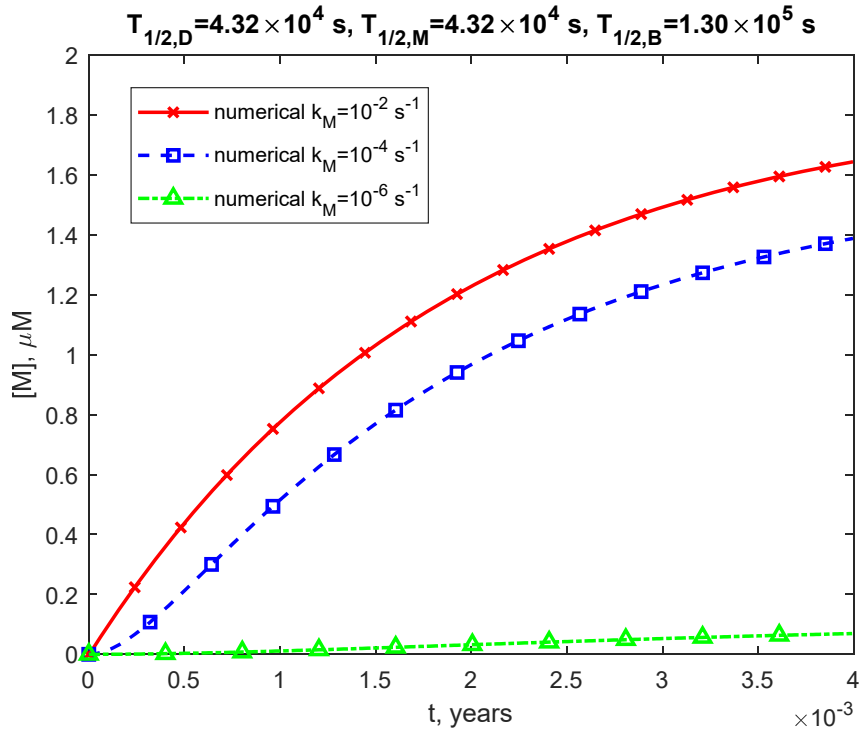

Fig. S17. (a) Molar concentration of TDP-43 monomers, [*M*], over time (in years). (b) Similar to Fig. S17a but focusing on a specific time range of [0 0.004 year] on the *x*-axis. The numerical solution is obtained by solving Eqs. (4)-(6) numerically with the initial condition (7). The presented scenario assumes physiologically relevant values for the half-lives of TDP-43 dimers, monomers, and aggregates. $T_{1/2,D} = 4.32\times10^4$ s, $T_{1/2,M} = 4.32\times10^4$ s, and $T_{1/2,B} = 1.30\times10^5$ s. The approximate solution is not displayed as it applies exclusively to the scenario involving infinite half-lives of TDP-43 dimers, monomers, and aggregates. The results are displayed for three values of k_M. $k_1 = 10^{-6}$ s^{-1} and $k_2 = 10^{-6}$ μM^{-1} s^{-1}.

(a)

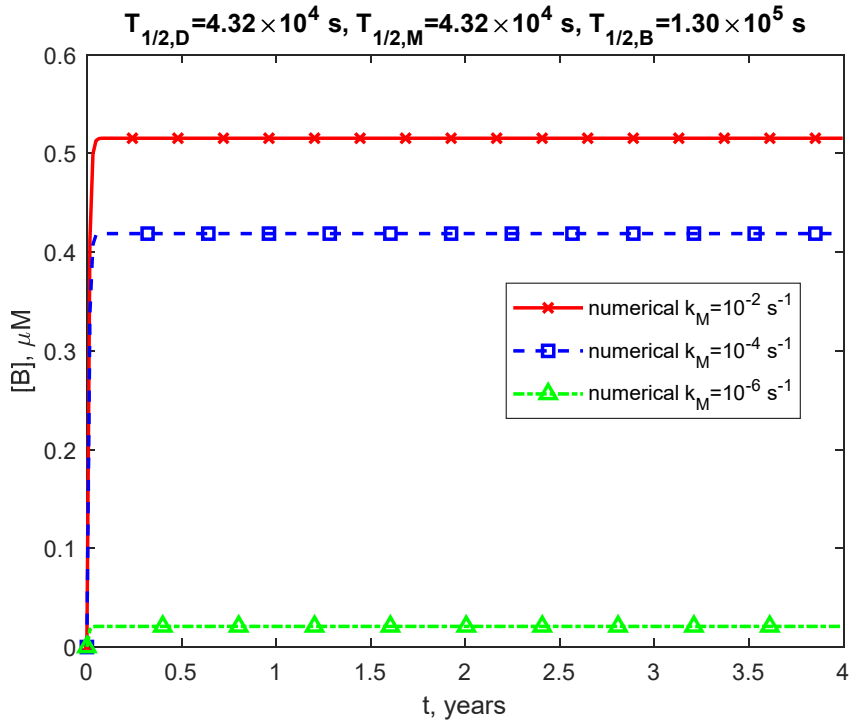

(b)

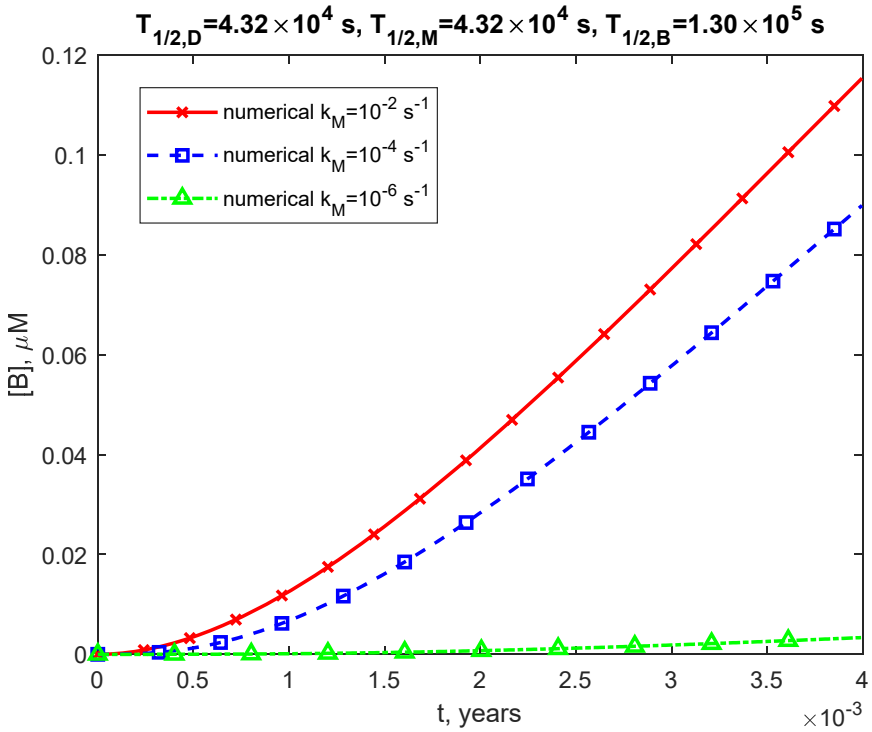

Fig. S18. (a) Molar concentration of TDP-43 aggregates, [*B*], over time (in years). (b) Similar to Fig. S18a but focusing on a specific time range of [0 0.004 year] on the *x*-axis. The numerical solution is

obtained by solving Eqs. (4)-(6) numerically with the initial condition (7). The presented scenario assumes physiologically relevant values for the half-lives of TDP-43 dimers, monomers, and aggregates. $T_{1/2,D} = 4.32 \times 10^4$ s, $T_{1/2,M} = 4.32 \times 10^4$ s, and $T_{1/2,B} = 1.30 \times 10^5$ s. The approximate solution is not displayed as it applies exclusively to the scenario involving infinite half-lives of TDP-43 dimers, monomers, and aggregates. The results are displayed for three values of k_M. $k_1 = 10^{-6}$ s^{-1} and $k_2 = 10^{-6}$ μM^{-1} s^{-1}.